

# *Spitzer* Observations of IC 348: The Disk Population at 2-3 Million Years.

Charles J. Lada, August A. Muench, K. L. Luhman, Lori Allen, Lee Hartmann, Tom Megeath, Philip Myers & Giovanni Fazio

*Harvard-Smithsonian Center for Astrophysics*

*Cambridge, MA 02138*

clada@cfa.harvard.edu, gmuench@cfa.harvard.edu, kluhman@cfa.harvard.edu  
lallen@cfa.harvard.edu, tmegeath@cfa.harvard.edu, pmyers@cfa.harvard.edu  
lhartmann@cfa.harvard.edu, gfazio@cfa.harvard.edu

Kenneth Wood

*School of Physics and Astronomy, University of Saint Andrews*

*Saint Andrews, KY 16 9SS, Scotland, UK*

kw25@st-andrews.ac.uk

and

James Muzerolle, George Rieke, Nick Siegler & Erick Young

*Steward Observatory, University of Arizona*

*Tucson, Az 85712*

jamesm@as.arizona.edu, grieke@as.arizona.edu, eyoung@as.arizona.edu

## ABSTRACT

We present near and mid-infrared photometry obtained with the *Spitzer Space Telescope* of  $\sim 300$  known members of the IC 348 cluster. We merge this photometry with existing ground-based optical and near-infrared photometry in order to construct optical-infrared spectral energy distributions (SEDs) for all the cluster members and present a complete atlas of these SEDs. We employ these observations to both investigate the frequency and nature of the circumstellar disk population in the cluster. The *Spitzer* observations span a wavelength range between 3.6 and 24  $\mu\text{m}$  corresponding to disk radii of  $\sim 0.1 - 5$  AU from the

central star. The observations are sufficiently sensitive to enable the first detailed measurement of the disk frequency for very low mass stars at the peak of the stellar IMF. Using measurements of infrared excess between 3.6 and 8  $\mu\text{m}$  we find the total frequency of disk-bearing stars in the cluster to be  $50 \pm 6\%$ . However, only  $30 \pm 4\%$  of the member stars are surrounded by optically thick, primordial disks, while the remaining disk-bearing stars are surrounded by what appear to be optically thin, anemic disks. Both these values are below previous estimates for this cluster. The disk fraction appears to be a function of spectral type and stellar mass. The fraction of stars with optically thick disks ranges from  $11 \pm 8\%$  for stars earlier than K6, to  $47 \pm 12\%$  for K6-M2 stars to  $28 \pm 5\%$  for M2 - M6 stars. The disk longevity and thus conditions for planet formation appear to be most favorable for the K6-M2 stars which are objects of comparable mass to the sun for the age of this cluster. The optically thick disks around later type ( $> M4$ ) stars appear to be less flared than the disks around earlier type stars. This may indicate a greater degree of dust settling and a more advanced evolutionary state for the late M disk population. Finally we find that the presence of an optically thick dust disk is correlated with gaseous accretion as measured by the strength of  $\text{H}\alpha$  emission. A large fraction of stars classified as CTTS possess robust, optically thick disks and very few of such stars are found to be diskless. The majority (64%) of stars classified as WTTS are found to be diskless. However, a significant fraction (12%) of these stars are found to be surrounded by thick, primordial disks. These results suggest that it is more likely for dust disks to persist in the absence of active gaseous accretion than for active accretion to persist in the absence of dusty disks.

*Subject headings:* infrared: stars — circumstellar matter — open clusters and associations: individual (IC 348)

## 1. Introduction

Circumstellar disks are of fundamental importance for the physical processes of star and planet formation. During protostellar evolution, disks provide the primary channel for accreting interstellar gas and dust that ultimately make up a star. Circumstellar disks are also the formation sites of planetary systems such as our own solar system. Characterizations of the frequency and lifetimes of such disks is important for developing an understanding of disk evolution and planet formation. Circumstellar disks are most readily detected and identified by their infrared emission. In particular, the optical-infrared spectral energy distributions

(SEDs) of stars with circumstellar disks are expected to display a characteristic power-law shape or signature (e.g., Lynden-Bell & Pringle 1974). This expectation has been largely confirmed by observations (e.g., Rucinski 1986; Adams, Lada and Shu 1987, Beall 1987, etc.) Moreover, the detailed shape of a disk’s SED is also expected to be sensitive to the structure and mass of the disk (e.g., Adams, Lada & Shu 1988, Kenyon and Hartmann 1987, Wood et al 2001, etc).

Because of the difficulty in obtaining the sufficient wavelength coverage necessary to construct SEDs of disk-bearing stars, most statistical studies of the frequencies and lifetimes of circumstellar disks have relied on using measurements of infrared excess at a single wavelength (usually the longest wavelength permitted by ground based imaging systems, typically either 2.2 microns or 3.4 microns), as a proxy for disk identification. Measurements of such near-infrared excesses in embedded clusters have indicated high disk frequencies for the youngest stars but relatively short disk lifetimes (e.g., Haisch, Lada & Lada 2001a). However, ground-based measurements based on excess detection at a single wavelength in the near-infrared are inherently limited; they are useful for detecting the presence of disks but provide little information about the more detailed nature (mass, structure, etc.) of disks (Wood et al. 2001). Moreover, such measurements are subject to systematic uncertainties in such assumed parameters as the adopted intrinsic colors of stars and extinction law assumed and these uncertainties could directly impact the derived statistics. The *Spitzer* satellite has greatly improved the ability to confidently identify and study circumstellar disks by making it possible to obtain SEDs for young stellar objects over an interesting range of wavelength extending well into the mid-infrared wavelength bands in reasonable amounts of observing time (e.g., Hartmann et al. 2005; Sicilia-Aguilar et al. 2005). Mid-infrared wavelengths are ideal for studying disks because these wavelengths are well removed from the peak of the underlying stellar energy distribution resulting in much greater excesses over the underlying stellar photosphere.

As part of the *Spitzer* GTO program a number of young embedded clusters have been imaged with both the IRAC and MIPS cameras with the goal of investigating disk evolution. The first paper resulting from this program examined two clusters (Tr 37 and NGC 7160) of differing age (4 and 10 Myr respectively) but at the same distance (900 pc) from the sun (Sicilia-Aguilar et al. 2005). These clusters exhibited significantly different disk fractions (48% and 4%, respectively) suggesting significant disk evolution between 4 and 10 Myr in these systems. In addition evidence for disk evolution within the clusters was also suggested by the identification of a small but significant population of disk bearing stars with optically thin inner disk regions and infrared excesses only at wavelengths longward of  $4.5 \mu\text{m}$ . In this paper we present and analyze *Spitzer* observations of the IC 348 cluster which is the nearest (320 pc), relatively rich, embedded cluster to the sun and thus a prime target for the cluster

disk evolution program. Situated at one end of the Perseus molecular cloud complex, IC 348 is at an intermediate age (2-3 Myrs) for embedded clusters and only partially embedded in natal gas and dust. Its proximity has made it an important laboratory for investigating early stellar evolution and star formation. The cluster has been extensively studied and a great deal of effort has been directed toward determining its membership, primarily through spectroscopic investigations with the result that most of its members are likely known and confirmed (e.g., Luhman et al. 1998; 2003; 2005). The confirmed membership is relatively large ( $\sim 300$  stars) covering a wide range in mass from  $0.02$  to  $5 M_{\odot}$  with excellent statistical representation. Because of the cluster’s proximity, *Spitzer* observations enable us to accurately measure the frequency of infrared excess and circumstellar disks around the lowest mass stars down to and below the hydrogen burning limit. In this way we are able to obtain for the first time a robust disk census at the peak of the stellar IMF.

Previous studies of the disk population in this cluster have produced differing estimates of the disk fraction. Near-infrared *JHK* observations produced an estimate of the disk fraction of  $\sim 15\%$  for the population (Lada & Lada 1995) while longer wavelength *L* (3.4 microns) observations yielded a disk fraction of  $\sim 65\%$  for the 100 brightest members (Haisch, Lada & Lada 2001b). Similarly,  $H\alpha$  observations (Herbig 1998) appeared to suggest a disk fraction of  $\sim 50\%$ . At the same time searches for millimeter-wave continuum from disks in the cluster failed to detect a single disk suggesting that as a whole the disk masses in IC 348 were lower than those that characterize the Taurus cloud complex (Carpenter 2002).

In this paper we report new measurements on the disk fraction based on *Spitzer* satellite observations at 3.6, 4.5, 5.8, 8.0 and 24.0 microns using the IRAC and MIPS cameras. We are able to construct the SEDs of  $\sim 300$  confirmed members of the cluster and derive improved and more accurate disk frequencies enabling the investigation of disk evolution in considerable more detail than possible in previous studies.

## 2. Observations and Data Reduction

As a part of the Guaranteed Time Observations of the IRAC and MIPS instrument teams, we obtained images of IC 348 at 3.6, 4.5, 5.8, 8.0, and  $24 \mu\text{m}$  with IRAC and MIPS on the *Spitzer Space Telescope*. The IRAC data consisted of two separate observations, a large shallow map and a small deep map on 2004 February 11 and 18 (UT), respectively. The plate scale and field of view of IRAC are  $1''.2$  and  $5''.2 \times 5''.2$ , respectively. The camera produces images with FWHM =  $1''.6$ - $1''.9$  from 3.6 to  $8.0 \mu\text{m}$  (Fazio et al. 2004). The shallow map contained a  $6 \times 7$  mosaic of pointings separated by  $280''$  and aligned with the array axes. At each cell in the map, images were obtained in the 12 s high dynamic range mode,

which provided one 0.4 s exposure and one 10.4 s exposure. The map was performed twice with offsets of several arcseconds between the two iterations. The resulting shallow maps had centers of  $\alpha = 3^{\text{h}}43^{\text{m}}24^{\text{s}}$ ,  $\delta = 32^{\circ}07'03''$  (J2000) for 3.6 and 5.8  $\mu\text{m}$  and  $\alpha = 3^{\text{h}}44^{\text{m}}18^{\text{s}}$ ,  $\delta = 32^{\circ}13'47''$  (J2000) for 4.5 and 8.0  $\mu\text{m}$ , dimensions of  $33' \times 29'$ , and position angles of  $170^{\circ}$  for the long axes. The deep IRAC map contained a  $3 \times 3$  mosaic of pointings separated by  $290''$ . At each cell in the map, two 100 s images were obtained at each of eight dithered positions, resulting in a total exposure time of 1600 s for most of the map. The resulting deep maps had centers of  $\alpha = 3^{\text{h}}44^{\text{m}}44^{\text{s}}$ ,  $\delta = 32^{\circ}05'50''$  (J2000) for 3.6 and 5.8  $\mu\text{m}$  and  $\alpha = 3^{\text{h}}44^{\text{m}}37^{\text{s}}$ ,  $\delta = 32^{\circ}12'27''$  (J2000) for 4.5 and 8.0  $\mu\text{m}$ , dimensions of  $15' \times 15'$ , and position angles of  $79^{\circ}$ .

For each of the shallow and deep IRAC maps, the images from the *Spitzer* Science Center pipeline (version S10.5.0) were combined into one mosaic at each of the four bands using custom IDL software developed by Robert Gutermuth. Point sources in these data were identified with the task DAOFIND under the IRAF package APPHOT. Aperture photometry for these sources then was extracted with the task PHOT using a radius of two pixels ( $2''.4$ ) for the aperture and inner and outer radii of two and three pixels for the sky annulus. We selected these relatively small apertures and sky annuli to provide the best possible subtraction of background emission from the parent cloud of IC 348, which is bright and spatially variable at mid-IR wavelengths.

For an aperture radius of 10 pixels and a sky annulus extending from 10 to 20 pixels, we adopted zero point magnitudes ( $ZP$ ) of 19.670, 18.921, 16.855, and 17.394 in the 3.6, 4.5, 5.8 and 8  $\mu\text{m}$  bands, where  $M = -2.5 \log(DN/sec) + ZP$  (Reach et al. 2005). We then applied aperture corrections of 0.274, 0.298, 0.543, and 0.769 mag to the photometry. The photometry from the shallow and deep images were merged into one catalog. We used sources found in both catalogs to characterize our photometric uncertainties. A total of 764, 817, 308 and 223 overlapping sources were found in bands 1-4, respectively. Of these 84, 79, 90 and 83% had observed 1 sigma scatter less than 0.1 magnitudes. Only 1 – 2% of the overlap sources had 1 sigma variations which were greater than the 3 sigma predicted photometric errors calculated from the aperture photometry and which includes sky background, read and shot noise. These estimates of the photometric accuracy are particularly relevant for known cluster members, which fall predominately within this overlap region. In this combined data set, one bright star, HD 23180 ( $V = 3.9$ ), lacks unsaturated measurements at 3.6 and 4.5  $\mu\text{m}$ .

Observations of IC 348 using the Multiband Imaging Photometer for *Spitzer* (MIPS; Rieke et al. 2004) were taken in February 2004. The cluster was mapped using scan mode with 12 0.5-degree scan legs and half-array cross-scan overlap, resulting in a total map size of about 0.5 x 1.5 degrees including overscan and overlapping completely the IRAC

observations. The total effective exposure time per point at  $24\mu\text{m}$  is about 80 seconds. The MIPS images were processed using the instrument team Data Analysis Tool, which calibrates the data and applies a distortion correction to each individual exposure before combining into a final mosaic (Gordon et al. 2005). Point source photometry was performed on the  $24\mu\text{m}$  mosaic using PSF fitting with *daophot*. Except in a few cases where faint sources lay near bright extended background emission, the measurement errors are dominated by the 10% uncertainty in the absolute flux calibration. We do not consider data from the other two MIPS channels in this contribution.

### 3. Results

#### 3.1. Membership Sample

In this paper we consider only the observations of  $\sim 300$  cluster stars with confirmed membership by Luhman et al (2003). These cluster members were initially selected from a complete magnitude-limited sample of stars whose optical-infrared colors placed them above the main sequence for the distance of this cluster. Spectra and near-infrared photometry exists for a significant fraction of these candidate members. Membership for these stars was assessed on the basis of the following factors: known proper-motions, the presence of Li absorption, spectroscopic indication of low surface gravity, photometric evidence of extinction, presence of emission lines and/or infrared excess. The membership sample is thus not biased toward disk bearing stars since the selection was not limited to stars with observed signatures of disks such as emission-line or infrared-excess stars. The sample is known to be complete within a 16 by 14 arc minute region centered on the cluster for stars with masses greater than 0.03 solar masses and for visual extinctions less than 4 magnitudes (Luhman et al. 2003). This area encompasses 75% of the confirmed members examined in this paper. In Table 1 we present a catalog of the IRAC and MIPS photometry for all sources. We combined our *Spitzer* IRAC and MIPS data with ground-based near-infrared and optical observations from the literature to construct spectral energy distributions (SEDs) for all the sources in the catalog. We present an atlas of these SEDs for the members of IC 348 in Appendix A.

#### 3.2. Spectral Energy Distributions

The examination of the optical-infrared SED of a target star provides the most robust method for the identification of the presence of a circumstellar disk. The shape of the

SED can distinguish a disk origin for observed infrared excesses from other possible causes and moreover is sensitive to such parameters as disk structure, orientation and if extended to millimeter-wavelengths, the size distribution of emitting particles. A particularly useful measure of the shape of an SED is its slope (e.g., Lada 1987). Here we use the  $3.6 - 8.0 \mu\text{m}$  slope of the IRAC SED for each of the 263 sources in our catalog/atlas that was detected in all four IRAC bands to identify stars with disks and obtain a census of the circumstellar disk population in the cluster. We obtain our metric for the SED slope,  $\alpha$ , from a simple power-law, least-squares fit to the four IRAC bands for each star. The results of this procedure are shown in Figure 1 where we plot the slopes we derived for the stars in IC 348 as a function of spectral type. For reference we also derive the same diagram for stars in Taurus with published IRAC data (Hartmann et al. 2005).

In both clouds the sources primarily cluster around two distinct bands, one centered on an  $\alpha \approx -1.0$  and the other centered on an  $\alpha \approx -2.7$  corresponding to disk-bearing and diskless stars, respectively. Examination of the SED slopes in Taurus shows a distinct separation between objects within the two bands. This separation between diskless stars and disk-bearing stars has been noticed previously and has been interpreted to indicate a rapid transition between the two phases of evolution (Kenyon & Hartmann 1995; Wood et al. 2002). In the SED atlas in Appendix A we compare individual source optical-infrared SEDs to two disk models calculated from a Monte Carlo radiative transfer code (Bjorkman & Wood, 2001; Wood et al. 2002; Walker et al. 2004). The model disks extend from the dust destruction radius to 200 AU and are purely reprocessing disks with no accretion. For both models the disk mass is 3% of the stellar mass and the radial dependence of the disk surface density is  $\Sigma(r) \sim r^{-1}$ . The dust size distribution used in the models is described in Wood et al. (2002). One model is flared consistent with the requirements of vertical hydrostatic equilibrium while the other has a scale height reduced by a factor of 3 to approximate a disk which is spatially flatter as would be expected for a disk that has experienced significant mid-plane settling of its emitting dust. From a comparison of the observed SEDs, SED slopes and models we find that sources with disks that match the models (flared or flat) are characterized by  $\alpha > -1.8$ . From an examination of the SED slopes of apparently diskless stars in Taurus, we find that diskless stars (i.e., stellar photospheres) can be characterized by  $\alpha < -2.56$ . We note that the value of  $\alpha_{IRAC}$  for stellar photospheres can vary with spectral type. Indeed, we have examined the dependence of  $\alpha_{IRAC}$  on spectral type for dereddened diskless stars in Taurus and found that it can be well approximated by a linear function which is displayed in panels (A) and (B) of Figure 1. The variation in  $\alpha$  is small across the range of spectral types under consideration. Therefore for simplicity, we adopt a single photospheric value of  $\alpha_{IRAC,photosphere} = -2.56$ , which corresponds to the predicted slope for an M0 star (-2.66) plus a buffer of 0.1 to account for the typical precision of these SED

fits (See, for example, Table 2). Sources characterized by  $-2.56 < \alpha < -1.80$  we term anemic disks and are possibly transition objects, such as heavily depleted, optically thin disks, disks with inner holes, etc. (D’Alessio et al. 2005).

In Figure 2 we plot the median SEDs for each of the three SED types (thick disk, anemic disk, diskless photosphere) for the different spectral classes (See Appendix B for the derivation of IC 348 median SEDs). We note that anemic disks display very small excesses primarily only at the longest wavelengths and even where detected they typically have fluxes below that expected for an optically thick disk. Comparison with the median SED of Taurus disk-bearing stars with spectral types between K2-M0 indicates that for the stars in this spectral type range the circumstellar disks in IC 348 and Taurus are very similar in nature. Although for M0-M2 the median IC348 SED falls below the Taurus SED suggesting perhaps that some disk evolution or dust settling may have occurred in IC 348, similar to the situation in the 4 Myr cluster TR 37 (Sicilia-Aguilar et al. 2005).

We compute the disk fractions as a function of spectral type and mass and plot the result in Figure 3. Here we display the fraction of sources for which  $\alpha > -1.80$  (optically thick disks), the fraction of sources with  $-1.8 > \alpha > -2.65$  (anemic or thin disks) and the total disk fraction as a function of spectral type and stellar mass. The stellar mass is derived by converting the spectral types to effective temperatures using a subgiant temperature scale (Luhman 1999) and the effective temperatures to masses using the Baraffe et al. (1998) pre-main sequence evolutionary model calculations appropriate for a 2-3 Myr cluster. This is a satisfactory conversion for our purposes since at these ages nearly all these stars are on convective tracks in the HR diagram. The disk fraction appears to be a function of spectral type (mass). The disk fraction is lowest for stars with spectral types earlier than K6 and highest for stars with spectral types between K6-M2, that is, for stars with masses around 1 solar mass. For later spectral types there appears to be a definite decline in the disk fraction. Given the level of uncertainty on the individual points, the significance of this drop is difficult to assess. However the fact that the four contiguous lowest mass bins are systematically lower than the preceding two bins suggests that the fall off is real. To better assess the variation of disk fraction with spectral type we can calculate the disk fractions over wider intervals of spectral type and mass. More specifically, for all stars earlier than K6 we find disk fractions of  $11 \pm 8\%$  and  $8 \pm 8\%$  for optically thick disks and anemic disks, respectively. For stars between K6-M2 we find the corresponding disk fractions to be  $47 \pm 12\%$  and  $9 \pm 5\%$  and for stars between M2-M6 (which make up the last four bins of Figure 3) we find the corresponding disk fractions to be  $28 \pm 5\%$  and  $26 \pm 5\%$ . The decline of the optically disk fraction for the later spectral type/lowest mass stars is apparently significant. The fraction of all cluster members detected in all four IRAC bands with optically thick disks is found to be  $30 \pm 4\%$ , while the total disk fraction (optically thick + anemic disks)



for this population of sources is  $50 \pm 6\%$ . We note here that our disk census applies to the entire cluster membership. If we restrict our sample to only those cluster members located within the inner 16 by 14 arc min region of the cluster known to be complete for  $m_* > 0.03 M_\odot$  (Luhman et al. 2003), we derive nearly identical disk fractions as those computed above for the larger sample but with somewhat larger uncertainties.

### 3.3. *Spitzer* Color-Color Diagrams

In Figure 4 we plot the IRAC color-color diagram for the cluster. We have labeled the points in the figure with different symbols which correspond to stars whose IRAC SED slopes indicated whether they were diskless or surrounded by thick or anemic disks respectively. There is a continuous sequence in color from diskless stars to stars with progressively large excesses and increasingly substantial disks. The stars are clearly spatially segregated according to the nature of their surrounding disks, Unlike previous IRAC only studies of embedded clusters we find the gap between disk-bearing and diskless stars to be filled by stars with anemic disks.

Not all cluster members were detected in all IRAC bands, however, essentially all the members were detected at  $4.5 \mu\text{m}$ . Consequently, to obtain a more complete disk census for the entire cluster membership, we need to rely on analysis of shorter wavelength data and employ color-color diagrams. We have used the data in Table 1 to construct color-color diagrams combining *JHK* photometry with  $4.5 \mu\text{m}$  IRAC photometry for the IC 348 cluster members in order to identify sources with infrared excesses and compile a more complete excess/disk census for the cluster. Infrared excesses are derived in color-color diagrams from comparison of the observed colors with the intrinsic colors of normal diskless stars. We determined the intrinsic colors for the *Spitzer* bands by using *Spitzer* observations of Pleiades main-sequence stars (Stauffer 2005, private communication) and field M dwarfs (Patten 2005, private communication). In Figure 5 we present the  $J(1.25\mu\text{m})$ ,  $H(1.65\mu\text{m})$ ,  $K(2.2\mu\text{m})$ , B2 ( $4.5\mu\text{m}$ ) diagram for the cluster. Also plotted is the locus of main sequence dwarf stars and the reddening boundaries corresponding to three different spectral types (M0, M3, and M6). These boundaries are trajectories that parallel the reddening vector for stars of the differing spectral types. Although Figure 5 shows the reddening boundaries for three spectral types, we have calculated the total disk fraction for the cluster as a function of spectral type by using the appropriate reddening boundary for eight spectral type bins from A stars to late M stars and counting the number of stars to the right of that boundary. The disk fraction determined in this manner is plotted in Figure 6. The result for the entire population is very similar to that derived above using SED slopes for the somewhat

more restricted sample of sources detected in all four IRAS bands. This Figure confirms the decline in disk fraction with spectral type below a solar mass. The fact that the disk fraction derived in this way is lower than the total disk fraction from figure 3 indicates that most anemic disks do not show excess at  $4.5 \mu\text{m}$ . We did not calculate the disk fraction for stars later than M6 since this was done in an earlier contribution by Luhman et al. (2005) who employed IRAC only color-color diagrams to derive the disk fraction for the brown dwarf population in IC 348 from the *Spitzer* observations. They found the disk fraction for stars later than M6 to be  $42 \pm 13\%$ . This is higher than the disk fraction derived for the earlier type M stars and the cluster as a whole and may indicate a slight increase in the disk fraction below the hydrogen burning limit.

In figure 5 the stellar colors are plotted as different symbols with the filled circles representing stars found to have optically thick disks from analysis of their SEDs while the plus signs correspond to stars identified as possessing anemic disks. The diagram suggests that a reasonably accurate census of the thick disk fraction can be measured by adopting the M6 reddening boundary without consideration of the individual spectral types of the target stars. Thus if spectral types are not available using the  $JHK4.5\mu\text{m}$  color-color diagram with the M6 reddening boundary can produce a good estimate of the primordial disk fraction for a young stellar population.

The disk fractions we derive for the IC 348 cluster in Figure 6 are significantly lower than that ( $\sim 50\%$ ) derived by Haisch et al. (2001b) using ground-based  $L$  band observations in a similar analysis. The difference is attributable to two factors. First, Haisch et al. examined a magnitude limited ( $L < 12$  mag.) sample of 107 stars, about a third the size of the sample considered here. The *Spitzer* sample is dominated by late M stars which have a lower disk fraction than the K and early M stars that dominated the magnitude-limited Haisch et al. sample. Second, and more significant, is that there appears to be a difference in the observed  $3 \mu\text{m}$  colors of the stars in the two samples. If we examine the 95 sources in common between our two studies we derive a disk fraction of 36% from an analysis of the  $JHK \text{ IRAC } 3.6 \mu\text{m}$  color-color diagram using the same boundary for the reddening band as adopted by Haisch et al. This difference in derived disk fraction appears to be largely the result of the fact that the  $K - 3.6\mu\text{m}$  colors of the stars in the present study appear to be bluer than the  $K - L$  colors of Haisch et al. The origin of this difference is not clear but may be due to systematic calibration uncertainties the  $3.6 \mu\text{m}$  observations. However based on analysis of the stellar SEDs, it appears that the IRAC data produce the more a reliable measure of the disk/excess fraction.

In Figure 7 we plot an IRAC-MIPS color-color diagram for those sources in the cluster detected at  $24 \mu\text{m}$ . Different symbols represent the different disk types (thick and anemic) as

well as diskless stars as determined from IRAC colors. Sources with thin or anemic disks form a narrow band with little dispersion in 3.6-8.0  $\mu\text{m}$  color but a wide extent in 8.0 – 24.0  $\mu\text{m}$  color. This band forms the lower boundary to the extent of thick disk sources in this color-color plane. The distribution of anemic disk sources appears to be less concentrated in the 8 – 24  $\mu\text{m}$  color than that of the thick disk sources. For the anemic disks the contrast between inner and outer disk emission increases as the 8 – 24  $\mu\text{m}$  color increases. The six anemic sources with the largest 24  $\mu\text{m}$  excesses represent objects with the largest contrast between inner and outer disk emission and may be disks with significant inner holes. The majority of anemic disk sources do not appear to possess such significant inner holes.

We also note the presence in Figure 7 of two small groupings of stars whose 3.6 – 8.0  $\mu\text{m}$  color is close to zero magnitude. Eight out of nine of these stars show no indication of infrared excess in any of the IRAC bands, while one (source # 8, see Table 1) is identified as an anemic disk by its SED slope. Three of these sources have 8 – 24  $\mu\text{m}$  colors close to zero magnitude, characteristic of diskless photospheres out to 24  $\mu\text{m}$  wavelength. Two are G stars (#s 11 & 22) and one is a K star (# 10363). A fourth source, an A star (# 3), also exhibits a near photospheric 8 – 24  $\mu\text{m}$  color but appears to have a slight excess in the 24 $\mu\text{m}$  band. A second grouping of five stars is clustered around an 8 – 24  $\mu\text{m}$  color of  $\sim 1.4$  magnitudes. Four of these stars appear to be diskless in the IRAC bands but clearly exhibit excess at 24  $\mu\text{m}$ . Two of the stars are early type A stars (#s 7 & 25) while another is an F star (# 30) and one is a G star (#20). These stars could either be extreme examples of anemic (transiton) disks or very young debris disk systems. To distinguish between these two possible interpretations requires knowledge of whether the circumstellar material producing the 24  $\mu\text{m}$  excess is remnant primordial disk material or newly generated dust produced by collisions between planetesimals and this is very difficult to ascertain with the existng observations for such a young cluster.

## 4. Discussion

### 4.1. Disk Evolution

We have obtained a detailed census of circumstellar disks among the members of the IC 348 cluster using observations from the *Spitzer* Satellite coupled with extensive ground-based data from the literature. The total disk fraction for the cluster membership is found to be  $50 \pm 6\%$  but only  $30 \pm 4\%$  of the members bear optically thick primordial disks. Both these fractions are lower than previously estimated from ground-based  $L$  band observations, although they are consistent with a normal extrapolation of the measured ground-based K (2.2 $\mu\text{m}$ ) band excess fraction (Lada & Lada 1995). Our observations provide evidence

once again for rapid disk evolution in clusters. If all stars in this cluster started out with circumstellar disks, then our data indicate that between roughly 60 – 70% of the cluster members have lost their primordial disks in only 2-3 Myrs. However we also find that the disk fraction for this cluster is also a function of spectral type and thus stellar mass. The early type stars exhibit a very low disk fraction consistent with earlier findings (Haisch et al. 2001b) and suggesting that  $\sim 90\%$  of stars earlier than K6 have lost their disks in only 2-3 Myrs. The disk fraction peaks for late K and early M stars, which are solar mass objects at the age of the cluster and roughly 50% of these solar analogs have managed to retain their original disks over the lifetime of the cluster. Surprisingly the disk fraction drops for later spectral type stars that dominate the cluster membership. Only about 30% of these stars have retained optically thick disks, suggesting perhaps that their rate of evolution is between that of the early type stars and solar type stars.

An expected consequence of disk evolution is a change in disk structure due to the settling of small dust grains toward the disk midplane. This produces a reduction in the scale height of the emitting particles and an overall decrease in the level of excess emission across the disk SED. Recently evidence for such evolution in SEDs of young stars was obtained in Spitzer observations by Sicilia-Aguilar et al. (2005). These authors compared the SEDs of stars in three stellar groups of differing age, Taurus (1-2 Myr), Tr 37 (4 Myr) and NGC 7160 (10 Myr). In addition to the expected overall decrease in disk fraction with age, they found a correlation of disk flux or infrared excess with age, such that the stars that retained disks exhibited lower disk fluxes with increasing age. The disk fluxes at the shorter wavelengths, presumably from the inner disk regions, seemed to decrease more rapidly than those at the longest (i.e.,  $24\mu\text{m}$ ) wavelength. As mentioned earlier and shown in Figure 2, the median SED for IC 348 disk bearing stars is very similar to the corresponding median SED for Taurus sources, suggesting similar disk structure for corresponding sources in the two clouds. Thus, even though IC 348 has a lower overall disk fraction, its surviving disks do not seem significantly different in structure than those in Taurus.

In Figure 8 we display the SEDs of four sources taken from our atlas of SEDs as a representative sample of various SED shapes we find for cluster stars. These objects are of similar spectral type (M0 - M2) but exhibit different levels of infrared excess due to circumstellar disks. They range from a strongly flared disk to a diskless photosphere. These SEDs clearly represent systematically varying disk structure for sources within the cluster. For comparison appropriate synthetic stellar photospheres and two disk models of differing scale height but similar inclination (i.e.,  $i = 60^\circ$ ) are also plotted for each star (see Appendix 1 for details). Comparison with the model disks and photospheres suggests that the decrease in disk emission from top to bottom is likely a result of a change in disk scale height. This, in turn, may be a sign of disk evolution due to dust settling. If so, this suggests that the

rate of disk evolution can vary within a single, similarly aged, population of young stars. It is interesting in this regard that we find that for cluster members with spectral types earlier than M2, 70% of the disk-bearing stars have SEDs that closely match the prediction of the most flared model disk (i.e., the upper disk model curve in Figure 8) while 90% of the disk-bearing stars with spectral types later than M4 exhibit SEDs that lie below this model, coincident with or slightly above the prediction of the reduced scale height disk model (i.e., the lower disk model curve). Thus the disks around the lowest mass, late-type stars are flatter and presumably more evolved than the disks around the earlier type and solar mass stars. This is interesting given that the disk fraction around these later type stars is also lower or more evolved than that for the solar mass stars in the cluster. However, it is interesting to note here that modeling of disks around brown dwarfs in Ophiuchus also suggested flatter disk structure for such very low mass objects (Natta et al 2002). The rapid disk evolution times suggested by our observations are a challenge for theories of planet formation which typically require periods of order  $10^7$  years or longer to build Jupiter mass objects. However, our data also suggest that the disk evolution time scale is a function of stellar mass and may peak for stars similar in mass to the sun. Thus in IC 348 the conditions for planet building may be most favorable around stars with masses similar to our sun.

We have so far considered the properties of optically thick disks which are likely to be primordial, protoplanetary disks. We have also identified a population of anemic or optically thin disks in the cluster. These disks appear to be typically detected only at the longest wavelengths, 8 and  $24\mu\text{m}$ . The fraction of sources surrounded by such disks ranges from about 8% for the earliest type stars to 25% for the later type stars. However while such anemic disks are a small portion of the disk-bearing early-type (<K6) stars, they represent a large fraction (1/2) of the disk-bearing late-type (>M3) stars. This perhaps is another indication of more advanced evolution for the disks around lower mass stars.

Source 72, whose SED is shown in Figure 8, is an interesting object because it is an example of an anemic disk whose  $24\mu\text{m}$  (outer disk) emission is as bright as that from the thick and flared primordial disks shown in the upper two panels of Figure 8. This suggests the presence of a significant inner disk hole with a fairly pronounced ring of outer disk emission. Examination of the SEDs in the atlas suggests that the evolution from a flared to a flat disk structure that is implied by the arrangement of SEDs in Figure 8 is fairly typical in that the  $24\mu\text{m}$  flux almost always drops with the fluxes at shorter wavelengths. This is consistent with what one might expect if disks evolved more or less homologously (e.g., Wood et al. 2002). Sources such as 72 represent an exception. Their strong excess at  $24\mu\text{m}$  could either result from a sequence of inside-out evolution in which the dust in the outer disk remained puffed up as the dust in the inner disk rapidly settled or perhaps a sequence in which dust in the outer disk first settled to the mid-plane and then later was puffed up again as the inner

disk cleared.

Only 37% of the anemic disk sources have been detected at  $24 \mu\text{m}$ . These are the sources identified in the IRAC-MIPS color-color diagram (Figure 7). This low detection fraction is the result of inadequate sensitivity at  $24 \mu\text{m}$  and so these particular sources are clearly the objects with the largest  $24 \mu\text{m}$  excesses among the anemic disk population. Only 6 (or 33%) of these sources exhibit  $8 - 24 \mu\text{m}$  colors as extreme as Source 72. The remaining anemic sources have  $8 - 24 \mu\text{m}$  colors which span a similar range as those of optically thick disks. In addition, examination of the individual SEDs shows that about half the anemic disks detected at  $24 \mu\text{m}$  appear to be thin at  $24 \mu\text{m}$ . These facts suggest that most disks may undergo substantial evolution without developing significant inner holes, that is, the inner and outer regions are more or less simultaneously being depleted by the evolutionary process. However, it is not clear from our observations whether the rates of inner and outer disk evolution could still differ somewhat for these sources.

The data we have analyzed and discussed provides insights into inner (.1 - 5.0 AU) disk evolution as traced by small dust grains. It is not clear whether the evolution of the gaseous component of the disk proceeds in a similar manner or on a similar timescale. One proxy for tracing the evolution of the gas is via measurements of disk accretion onto the central star via observation of atomic emission lines. In particular the  $\text{H}\alpha$  emission is thought give an indication of the level of disk accretion onto the star. Indeed, Hartigan et al. (1990) found a correlation between optical veiling, which is an indirect measure of accretion, and  $\text{H}\alpha$  emission. Moreover these authors also found a correlation between veiling and infrared excess implying a correlation between the presence of a dust disk and  $\text{H}\alpha$  emission strength. A similar result was found by Hartmann (1998) who showed that stars with strong  $\text{H}\alpha$  emission in Taurus tended to have large K-L infrared excess. In Figure 9 we compare the  $\text{H}\alpha$  equivalent widths with the IRAC SED slopes of stars in the cluster. Typically an equivalent width of 10 Angstroms is taken to be indicative of the presence of accretion and stars with equivalent widths greater than this are designated as CTTS (classical T Tauri stars). Sources with smaller equivalent widths are designated as WTTS (weak-lined T Tauri stars) and are believed to be non-accreting objects or objects with very low accretion rates. This boundary between accretion and chromospheric emission is somewhat arbitrary and likely is not exactly appropriate for either very early or very late type stars. (For example, White and Basri (2003) suggest that for stars between K0 and K5 the boundary should be near 3 Angstroms; only three of stars in our sample earlier than K7 have equivalent widths between 3-10 Angstroms.) Figure 9 shows a definite correlation between  $\text{H}\alpha$  equivalent width and SED slope. In particular sources with slopes ( $> -1.8$ ) indicative of optically thick circumstellar disks have the strongest emission lines. Of the stars classified as CTTS and actively accreting objects, 68% possess optically thick disks and 11% are associated with

thin or anemic disks. Of the stars classified as non-accreting WTTS, 12% are associated with robust optically thick disks and 22% with thin disks. These data are not consistent with the notion that gaseous accretion disks exist for significant periods of time after the small dust emitting grains have gone away. This suggests that the gaseous and dust components of disks evolve on similar time scales. Indeed, it appears more likely that dust disks can persist for at least some time after gaseous accretion has been terminated.

## 5. Summary and Conclusions

We have combined *Spitzer* GTO and existing ground-based, optical-infrared observations to obtain an accurate census and investigate the nature of the disk population of the young embedded cluster, IC 348. We have constructed optical-infrared SEDs for all known members of the cluster spanning a spectral type range from A0 to M8. This range includes stars at and somewhat below the hydrogen burning limit. From analysis of these results we summarize our primary findings as follows:

1)- From analysis of the optical-infrared SEDs of the cluster members we determine the fraction of disk-bearing stars to be  $50 \pm 6\%$ . However only  $30 \pm 4\%$  of the member stars are surrounded by robust, optically thick or primordial disks while 20% of the member stars are surrounded by optically thin or anemic disks. These measurements are lower than previous estimates for this cluster. These measurements suggest that in the 2-3 Myr since the cluster formed, 70% of the stars have lost all or most of their primordial circumstellar disk material.

2)- The disk fraction is a function of spectral type. The lowest disk frequency is found for early type stars. Only  $11 \pm 8\%$  of stars earlier than K6 possess optically thick disks. The disk fraction peaks for stars of K6-M2 spectral types. These PMS stars have masses similar to the sun and the fraction of such stars with robust, thick disks is  $47 \pm 12\%$ . For M2-M6 stars the overall disk fraction is found to decline to a value of  $28 \pm 5\%$ . Thus it appears that disk longevity and the conditions for planet formation are most favorable around the solar mass stars in this cluster.

3)- The optically thick disks around the lower mass, later type ( $> M4$ ) stars in the cluster appear to be spatially flatter than those around the earlier type stars. This may indicate a greater degree of dust settling and more advanced evolution in the disks associated with the late M population.

4)- A population of optically thin or anemic disks is identified. The fraction of stars accompanied by such disks ranges from  $8 \pm 8\%$  for early type stars to  $26 \pm 5\%$  for M type stars. However the fraction of disk-bearing stars with anemic disks is small for stars earlier

than K6, but is roughly 50% for M stars. These disks are almost exclusively detected at the longest wavelengths  $\lambda \geq 8 \mu\text{m}$  corresponding to the outermost disk regions probed by the *Spitzer* observations. We find that 37% of the anemic disk population is detected in the MIPS  $24\mu\text{m}$  band. In a few cases the  $24\mu\text{m}$  emission is as strong as that predicted for a flared, optically thick disk suggesting that dust emission from the outer disk may persist or even strengthen in spite of significant inner disk evolution and dissipation. However, for most anemic disk sources detected at  $24 \mu\text{m}$ , the data are consistent with the possibility that the inner and outer disk regions (as traced by *Spitzer*) evolve homologously and are more or less simultaneously depleted of dusty material as they age.

5)- We find that the presence of an optically thick primordial disk is correlated with gaseous accretion as measured by  $\text{H}\alpha$  emission. A large fraction (68%) of stars classified as CTTS (by their measured  $\text{H}\alpha$  equivalent widths) are surrounded by robust primordial disks. Few such stars are diskless. On the other hand, 12% of the stars classified as WTTS are associated with thick disks, while 64% appear to be diskless. This result suggests that active accretion and the evolution of the dust disks are strongly coupled. It is more likely for dust disks to persist after active accretion ceases than for active accretion to persist after the dust disks disappear.

This work is based on observations made with the *Spitzer Space Telescope*, which is operated by the Jet Propulsion Laboratory, California Institute of Technology under NASA contract 1407. Support for this work was provided by NASA through contract 1256790 issued by JPL/Caltech. Support for the IRAC instrument was provided by NASA through contract 960541 issued by JPL. K. L. was supported by grant NAG5-11627 from the NASA Long-Term Space Astrophysics program. We thank an anonymous referee for a careful reading of the paper and thoughtful suggestions which improved its structure.

### A. Atlas of Spectral Energy Distributions for IC 348

We present an atlas of *observed* spectral energy distributions for 307 sources in the IC 348 cluster, including 304 previously identified members. The atlas is ordered by member spectral type. Seven members in very close binary pairs (9012, 9042, 9099, 22021, 30190, 30191, 30192) were excluded from this atlas since they only have photometry at optical wavelengths. Three sources classified as background stars based on their subluminous location in optical-infrared color-magnitude diagrams have spectral energy distributions suggesting they are in fact young stellar objects; we include these at the end of the atlas. Other than shifting the spectral energy distributions to a distance of 10pc (from 320pc assumed) the



monochromatic fluxes shown in the atlas are unmodified from the observations. *MIPS* 24  $\mu\text{m}$  upper limits are shown as open circles; these upper limits correspond to the net aperture flux within a 4.5'' aperture centered on each undetected star plus two times the noise, which includes photon and sky noise at that location on the image. This is the same definition for upper limits as used by the 2MASS survey. The references for the optical/near-infrared photometry used to create these SEDs as well as the passband to flux density conversions are listed in Table 4. In the optical, all the observed passbands were originally quoted as being  $VR_cI_c$ . All the near-infrared data were originally zeropoint calibrated to 2MASS, hence we adopt the 2MASS flux calibration.

Each SED in the atlas is fit by a reddened model atmosphere. The reddening law is a merger of empirical laws from Cardelli et al. (1989) for  $\lambda < 1\mu\text{m}$ ,  $R_V = 3.1$ ) and from a *Spitzer* study by Indebetouw et al. (2005) for  $1 < \lambda < 8\mu\text{m}$ . The extinction law (Case B,  $R_V = 5.5$ ) of Weingartner & Draine (2001) was used longward of  $8\mu\text{m}$ . A model atmosphere appropriate to each star was assigned based upon the IC 348 member’s spectral type and a conversion to effective temperature for pre-main sequence late-type subgiants from Luhman (1999). Members without spectral types (e.g., continuum sources) were assigned a 3900K (K7) model atmosphere. Model atmospheres were taken from the Nextgen database for a surface gravity appropriate for PMS stars ( $\log g = 4$ ) except for the centrally located (and poorly fit) B5 source #1 for which we used a model atmosphere for 15600K dwarf taken from Kurucz (1993). For each star, the model atmosphere was reddened and fit to the observed SED using an iterative filter convolution and  $\chi^2$  minimization routine; the fit range was from 0.5 to 2.0  $\mu\text{m}$  except for the latest spectral types, where we restricted the fit range to 0.7 to 2.0  $\mu\text{m}$ . Normalization was to the  $J$  passband. The derived  $A_V$  have a precision of 0.1 mag, though this is dependent upon the accuracy of the model atmospheres; we list the derived  $A_V$  in Table 2. Note that a more refined 5+ parameter model SED fit that includes effective temperature, reddening, surface gravity, rotation and accretion luminosity might result in improved fits to the IC 348 members’ blue optical SEDs. Including the effects of rapid rotation and accretion related blue excess (veiling) in the optical, might clarify whether or not some of the poor matches in the optical SED were due to these effects or a lack of precision in the assigned spectral type. However, such fits are beyond the scope of the present investigation.

For stars later than F type the SEDs are compared to two disk models both assuming a “typical” inclination, i.e.,  $\cos i = 0.5$ . The stellar parameters of the disk models were varied as a function of each star’s spectral type. Specifically, the disk models we show appropriately correspond to G3, K2, K7, M1, M2 or M5 photospheres; the latter star+disk models were used for all members later than M5, including the brown dwarf SEDs. The disk models shown are not fit to the observed SEDs; they are simply reddened by the  $\chi^2$  minimized  $A_V$

derived above and normalized to  $J$  band using filter convolution. Brief astrographical data is given for each star in the atlas, including its catalog number, spectral type, membership criteria and emission line properties. The reddening ( $A_V$ ) to a star as measured by the fit model atmosphere is listed as is the observed slope of the *IRAC* spectral energy distribution ( $\alpha_{IRAC}$ ). These values are also listed in Table 2.

We note a few individual sources:

**746, 2096, 212** These sources were previously thought to be background to the IC 348 cluster. Though 212 clearly appears to have an evolved “anemic” type disk and could be an interloper from a previous epoch of star formation (Perseus OB2, for example) the other two M5-M6 sources have very strong disk signatures. That their bolometric luminosities are more than 1 order of magnitude lower than comparable M5-M6 stars suggests that they are probably seen nearly edge-on (D’Alessio et al. 1999), explaining why they were not included in previous census.

**276, 203, 435** The *IRAC*-*MIPS* SEDs of these sources suggest that they are the best candidate IC 348 Class I sources with known spectral types. That they also have very low measured  $A_V$  suggests their optical colors are contaminated by scattered light (cf. 203).

## B. Median Observed Spectral Energy Distributions

We know a priori that the observed spectral energy distributions of very young stellar objects probably do not correspond to those of typical main sequence dwarfs for three straightforward reasons: 1) very young PMS star SEDs are distorted by the reradiation of stellar light by a circumstellar disk, 2) their SEDs can be distorted by rapid rotation and/or active chromospheres (Stauffer et al. 2003) and 3) the large radii intrinsic to contracting PMS stars requires that they have more giant-like surface gravities. Empirically we know that the latest spectral classes correspond to subgiant gravities (Luhman 1999) and display unusual optical colors Rebull et al. (2000). Sorting out the shape of the spectral energy distribution of young stars requires a set of sources with refined photometry covering the optical and mid-IR and with excellent spectral types. The ensemble of data we have collected for IC 348 satisfies those requirements probably better than any other young stellar cluster or star forming region; further, the *Spitzer* data presented here allows us to parse diskless stellar photospheres from disked stars with excellent precision. Typical photospheric SEDs for IC 348 stars would provide a good starting place for detailed tests of model atmospheres.

Another valuable reason for deriving the typical SEDs of IC 348 stars is to model the evolution of circumstellar disks. Recent comparisons of star-disk spectral energy distribution as a function of age have sketched a steady decrease in the disk flux in the IRAC bands for accreting classical type T-Tauri stars (Sicilia-Aguilar et al 2005) over a 10 Myr period. Placing the typical SEDs from IC 348 into such a sequence may prove useful for refining both time and environmental variations in inner disk properties; moreover, no other young cluster dataset probes a statistically significant population of sources down to and below the hydrogen burning limit as we have collected for IC 348.

Given our goal of providing median SEDs that correspond to the typical observed star or star/disk system in the 2-3 Myr IC 348 cluster, we present in Figure 2 median spectral energy distributions for diskless stars in IC 348, members with anemic disks and members with thick disks, while breaking the ensemble population into ten spectral type bins. Additionally and for the reasons listed above, deriving and publishing de-reddened ( $A_V = 0$ ) median SEDs for IC 348 would be an imprecise goal since the only obvious templates for dereddening would be dwarf SEDs. Instead we used the observed fact that the reddenings toward stars in IC 348 are typically low ( $A_V \sim 2$ ) to derive median *typical, observed* SEDs for each spectral type range.

Our prescription for deriving these median SEDs is as follows. Simply, a median filter was passed over the set of observed SEDs in a spectral type range to essentially select that “star” whose SED is typical of that spectral class. To parse the different star/disk classes, each observed SED in the spectral subclass was reddened **or** de-reddened to match the optical portion of this typical SED; then they were normalized to match the typical SED’s  $J$  band flux. Next, the IRAC SED slopes were measured and the three classifications of star/disk systems (star, anemic and thick) were parsed according to the  $\alpha_{IRAC}$  ranges given in Section 3.1. Note that these are not the origin of the observed and de-reddened  $\alpha_{IRAC}$  listed in Table 2; see Appendix A. Finally, each set of star/disk normalized SEDs were median filtered by bandpass to yield the median SEDs plotted in Figure 2 and the values given in Table 3. In this Table we list the relevant numerical data for these median SEDs (for each spectral type bin and star/disk system), including the median magnitudes and fluxes for each SED, the  $1\sigma$  dispersion in the fluxes and the number of data points that went into each median SED point.

Finally, we believe that the resulting median observed SEDs are reddened by approximately  $A_V \sim 2.5$ ; for example, the Taurus median SED (D’Alessio et al. 1999) compared to the IC 348 K6–M0 and M0–M2 spectral class SEDs in Figure 2 were arbitrarily reddened by  $A_V = 2.5$ ; yielding the excellent SED agreement shown in those panels.

## REFERENCES

- Adams, F. C., Lada, C. J., & Shu, F. H. 1987, *ApJ*, 312, 788
- Adams, F. C., Shu, F. H., & Lada, C. J. 1988, *ApJ*, 326, 865
- Baraffe, I., Chabrier, G., Allard, F., & Hauschildt, P. H. 1998, *A&A*, 337, 403
- Beall, J. H. 1987, *ApJ*, 316, 227
- Bessell, M. S., & Brett, J. M. 1988, *PASP*, 100, 1134
- Bessell, M. S., Castelli, F., & Plez, B. 1998, *A&A*, 333, 231
- Bjorkman, J. E., & Wood, K. 2001, *ApJ*, 554, 615
- Cardelli, J. A., Clayton, G. C., & Mathis, J. S. 1989, *ApJ*, 345, 245
- Carpenter, J. M. 2002, *AJ*, 124, 1593
- Cohen, M., Megeath, S. T., Hammersley, P. L., Martín-Luis, F., & Stauffer, J. 2003, *AJ*, 125, 2645
- Cohen, M., Wheaton, W. A., & Megeath, S. T. 2003, *AJ*, 126, 1090
- Cutri, R. M., et al. 2003, *VizieR Online Data Catalog*, 2246, 0
- D'Alessio, P., Calvet, N., Hartmann, L., Lizano, S., & Cantó, J. 1999, *ApJ*, 527, 893
- D'Alessio, P., et al. 2005, *ApJ*, 621, 461
- Draine, B. T. 2003, *ARA&A*, 41, 241
- Fazio, G. G., et al. 2004, *ApJS*, 154, 10
- Gordon et al. 2005, *PASP*, in press.
- Haisch, K. E., Lada, E. A., & Lada, C. J. 2001a, *ApJ*, 553, L153
- Haisch, K. E., Lada, E. A., & Lada, C. J. 2001b, *AJ*, 121, 2065
- Hartigan, P., Hartmann, L., Kenyon, S. J., Strom, S. E., & Skrutskie, M. F. 1990, *ApJ*, 354, L25
- Hartmann, L. 1998, *Accretion Processes in Star Formation*, (Cambridge University Press: Cambridge), p. 124.

- Hartmann, L., Megeath, S.T., Allen, L., Luhman, K., Calvet, N., D'Alessio, P. Franco-Hernandez, R., & Fazio, G. 2005, ApJ, in press.
- Herbig, G. H. 1998, ApJ, 497, 736
- Indebetouw, R., et al. 2005, ApJ, 619, 931
- Kenyon, S. J., & Hartmann, L. 1987, ApJ, 323, 714
- Kurucz, R. 1993, ATLAS9 Stellar Atmosphere Programs and 2 km/s grid. Kurucz CD-ROM No. 13. Cambridge, Mass.: Smithsonian Astrophysical Observatory, 1993., 13,
- Lada, C. J. 1987, IAU Symp. 115: Star Forming Regions, 115, 1
- Lada, E. A., & Lada, C. J. 1995, AJ, 109, 1682
- Luhman, K. L., Rieke, G. H., Lada, C. J., & Lada, E. A. 1998, ApJ, 508, 347
- Luhman, K. L. 1999, ApJ, 525, 466
- Luhman, K. L., Stauffer, J. R., Muench, A. A., Rieke, G. H., Lada, E. A., Bouvier, J., & Lada, C. J. 2003, ApJ, 593, 1093
- Luhman, K. L., Lada, E. A., Muench, A. A., & Elston, R. J. 2005, ApJ, 618, 810
- Luhman, K. L., Lada, C. J., Hartmann, L., Muench, A. A., Megeath, S. T., Allen, L. E., Myers, P. C., Young, E., Fazio, G. G. & Rieke, G. H. 2005, submitted.
- Lynden-Bell, D., & Pringle, J. E. 1974, MNRAS, 168, 603
- Muench, A. A., et al. 2003, AJ, 125, 2029
- Natta, A., Testi, L., Comerón, F., Oliva, E., D'Antona, F., Baffa, C., Comoretto, G., & Gennari, S. 2002, A&A, 393, 597
- Reach, W. T., et al. 2005, PASP, in press
- Rebull, L. M., Hillenbrand, L. A., Strom, S. E., Duncan, D. K., Patten, B. M., Pavlovsky, C. M., Makidon, R., & Adams, M. T. 2000, AJ, 119, 3026
- Rieke, G. H., et al. 2004, ApJS, 154, 25
- Rucinski, S. M. 1985, AJ, 90, 2321
- Sicilia-Aguilar, A., Hartmann, L., Calvet, N., et al. 2005, ApJ, in press.

Stauffer, J. R., Jones, B. F., Backman, D., Hartmann, L. W., Barrado y Navascués, D., Pinsonneault, M. H., Terndrup, D. M., & Muench, A. A. 2003, *AJ*, 126, 833

Walker, C., Wood, K., Lada, C. J., Robitaille, T., Bjorkman, J. E., & Whitney, B. 2004, *MNRAS*, 351, 607

Weingartner, J. C., & Draine, B. T. 2001, *ApJ*, 548, 296

White, R. J., & Basri, G. 2003, *ApJ*, 582, 1109

Wood, K., Lada, C. J., Bjorkman, J. E., Kenyon, S. J., Whitney, B., & Wolff, M. J. 2002, *ApJ*, 567, 1183

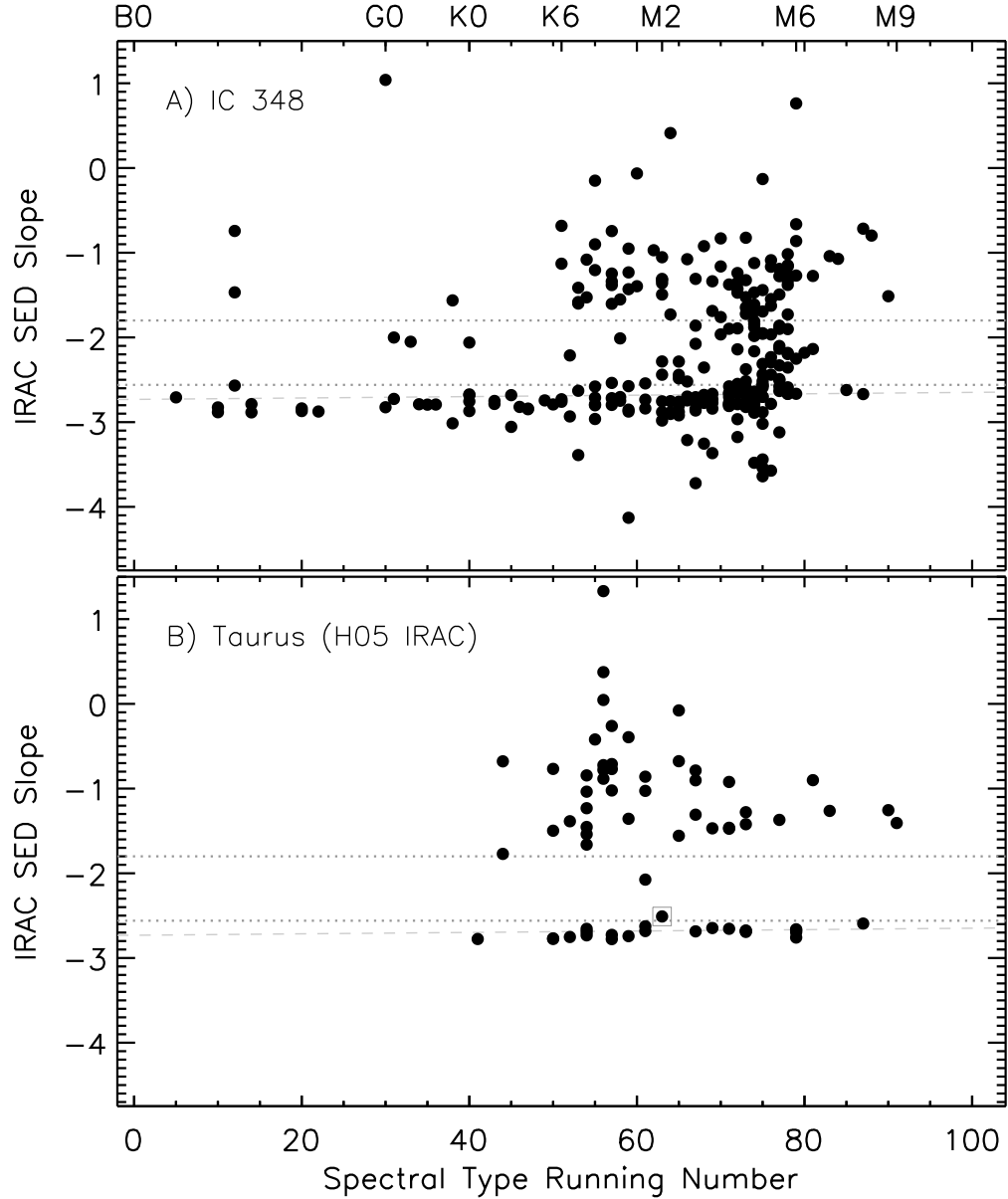


Fig. 1.— The dereddened power-law slopes of the IRAC SEDs for young stars plotted as a function of spectral type. A) Members of the IC 348 cluster; (B) the corresponding diagram for young stars in Taurus. Two prominent bands are observed in each diagram corresponding to stars with optically thick circumstellar disks and diskless stars. Stars whose slopes fall between the two bands are anemic disks or transition objects; for example, the Taurus M1.5 star CoKu Tau-4, which has been proposed to have an inner hole of radii 10 AU (D’Alessio et al. 2005), can be identified as such a transition object in panel (B), having an  $\alpha_{IRAC} = -2.51$  (open square). Data for Taurus stars taken from Hartmann et al. 2005 (H05).

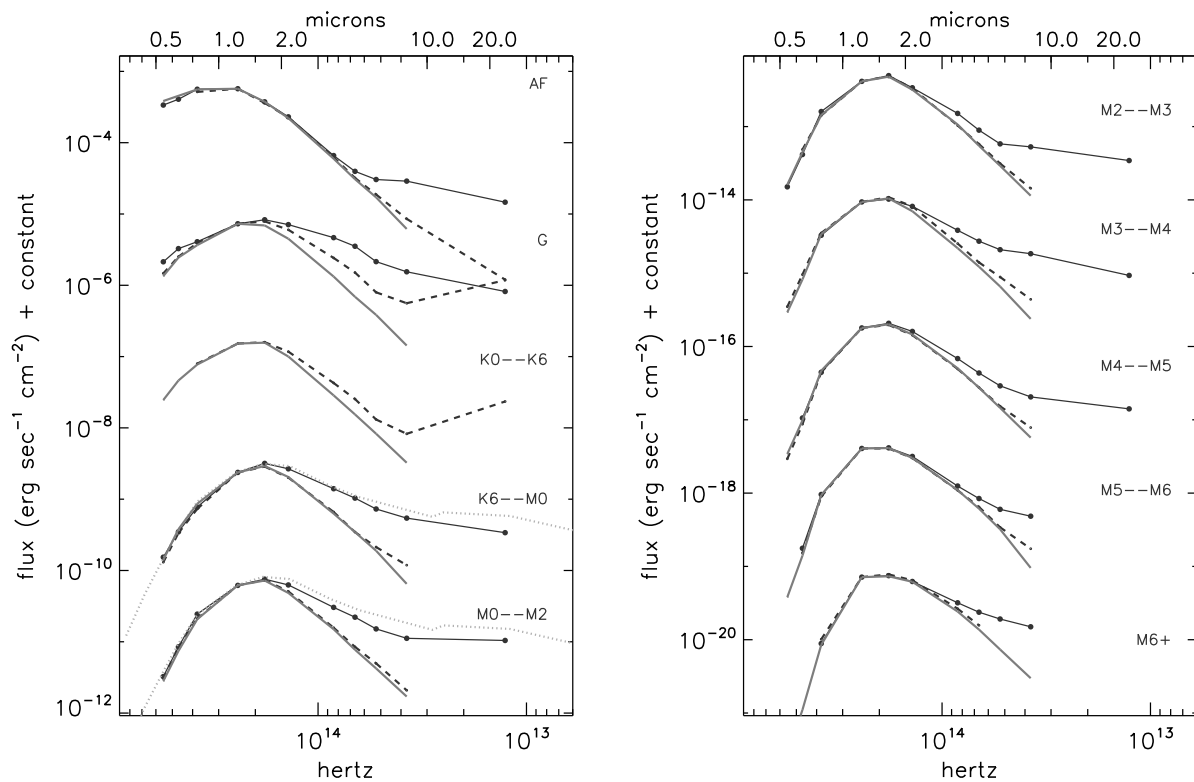


Fig. 2.— Median IC 348 SEDs for optically thick flared disks (solid colored line), anemic disks (dashed colored line) and diskless stellar photospheres (grey solid line) for the various spectral type bins. The median SED for K0-M2 classical T-Tauri stars in the Taurus cloud (D’Alessio et al. 1999) is also compared to the appropriate IC 348 SEDs. Note that these are the median *typical, observed* SEDs as a function of spectral type in IC 348 and thus do not correspond to  $A_V \neq 0$ ; see Appendix B.



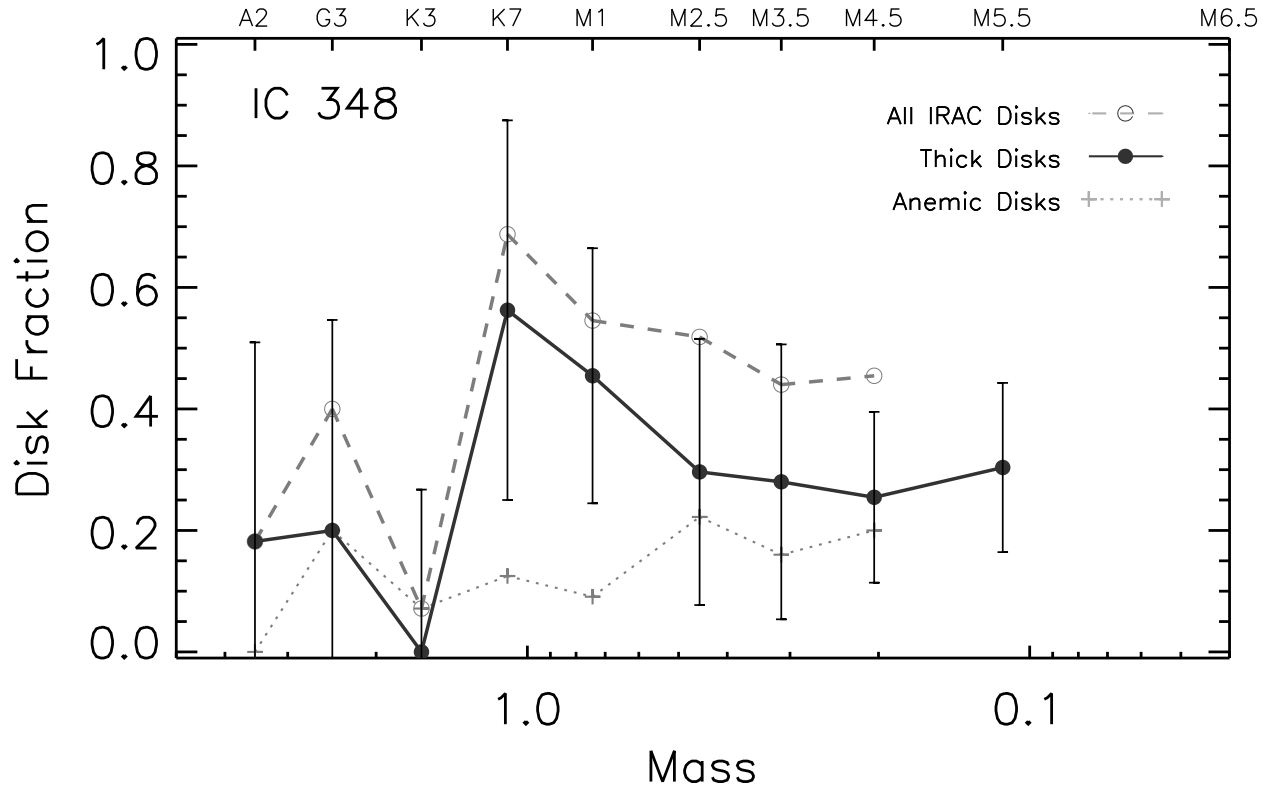


Fig. 3.— Disk frequency as a function of mass and spectral type as derived from analysis of the slopes of the IRAC SEDs for those cluster members detected in all four IRAC bands. See text. The solid line plots the disk fraction for stars with substantial optically thick disks, the lower dotted line plots the fraction of stars with anemic (possibly optically thin) disks. The dashed line on the top plots the total disk fraction (optically thick + anemic) for the cluster. The error bars represent simple poisson statistical uncertainties.

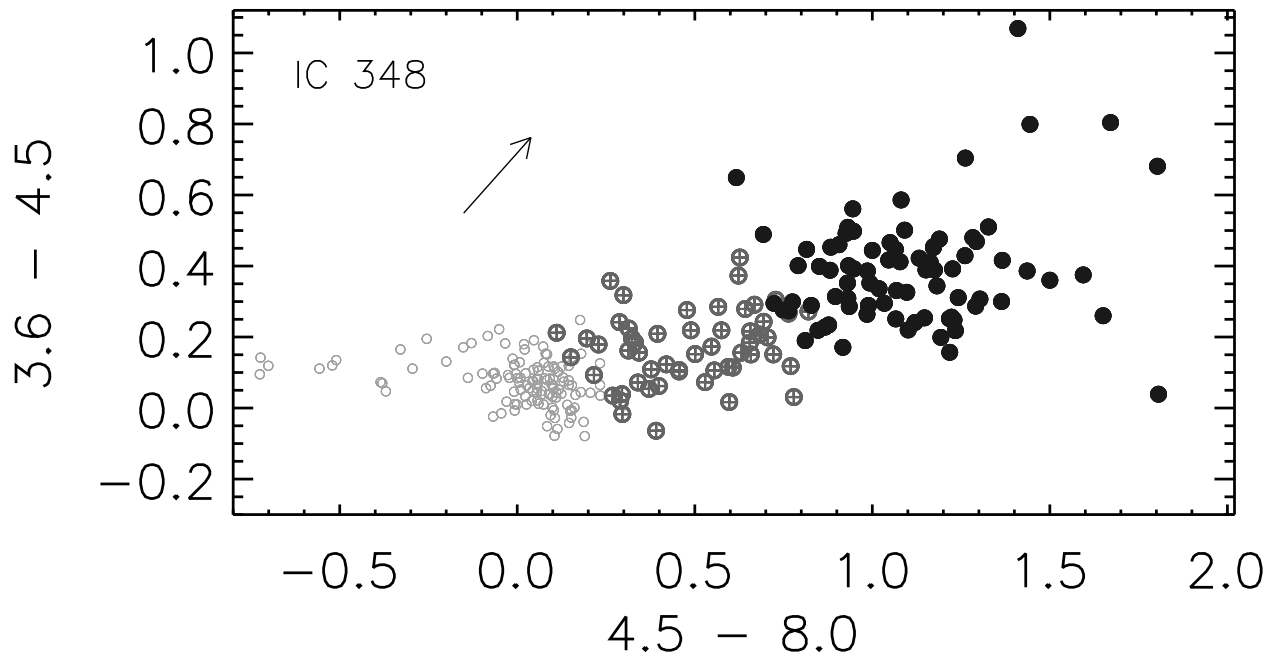


Fig. 4.— IRAC color-color diagram for IC 348 cluster members. The different symbols correspond to diskless stars (small open circles), anemic or thin circumstellar disks (circled crosses) and optically thick disks (filled circles) as defined by their IRAC SED slope. A reddening vector of length  $A_V = 20$  magnitude is shown.

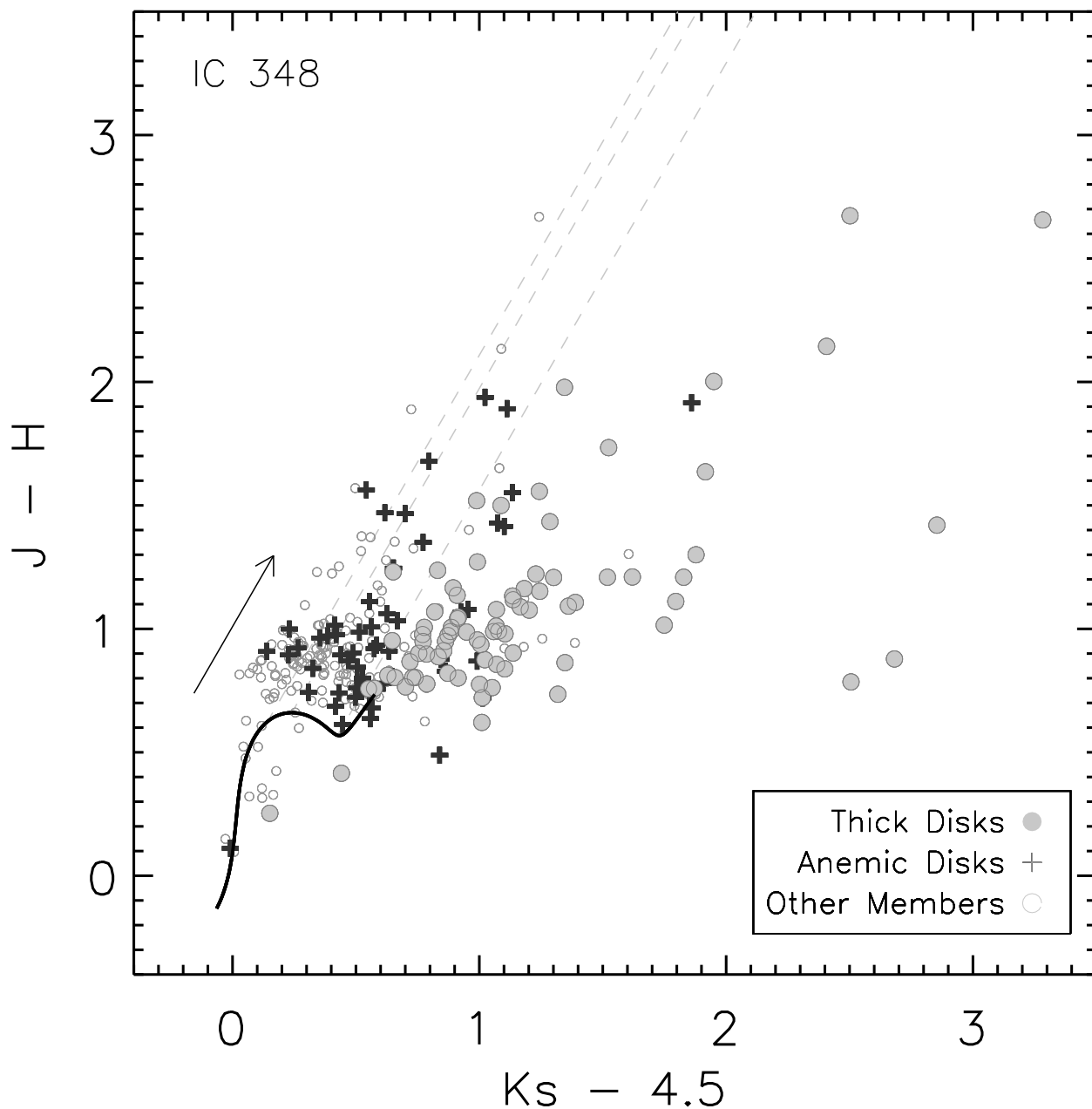


Fig. 5.— The  $J(1.25\mu\text{m})$ ,  $H(1.65\mu\text{m})$ ,  $K(2.2\mu\text{m})$ ,  $4.5\mu\text{m}$  color-color diagram for IC 348 cluster members. Sources are segregated based upon their *IRAC* SED slope; open circles correspond either to members without *IRAC* disk excess or to members lacking detections  $> 5\mu\text{m}$ . Also plotted are the locus of colors for main sequence stars (solid line) and the reddening boundaries (dashed lines) for three different dwarf spectral classes: M0, M3 and M6. These were derived by merging the *Spitzer* data from the Pleiades main-sequence stars (Stauffer 2005, private communication) and field M dwarfs (Patten 2005, private communication). A reddening vector of length  $A_V = 5$  is also shown.

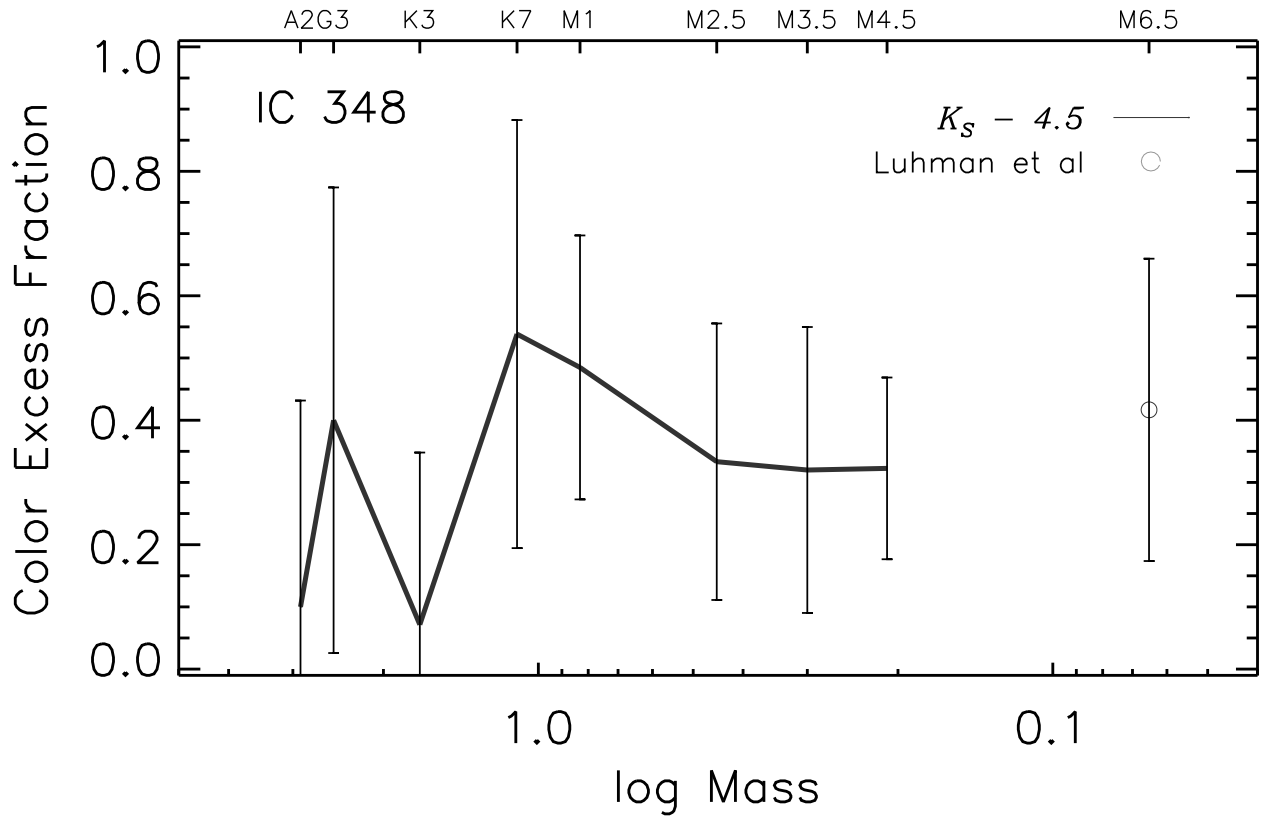


Fig. 6.— The disk frequency for IC 348 as a function of spectral type and mass derived from analysis of the  $JHK$   $4.5\mu\text{m}$  color-color diagram (Figure 5). The brown dwarf disk excess fraction from Luhman et al. (2005) with similarly derived error bars is plotted for comparison.

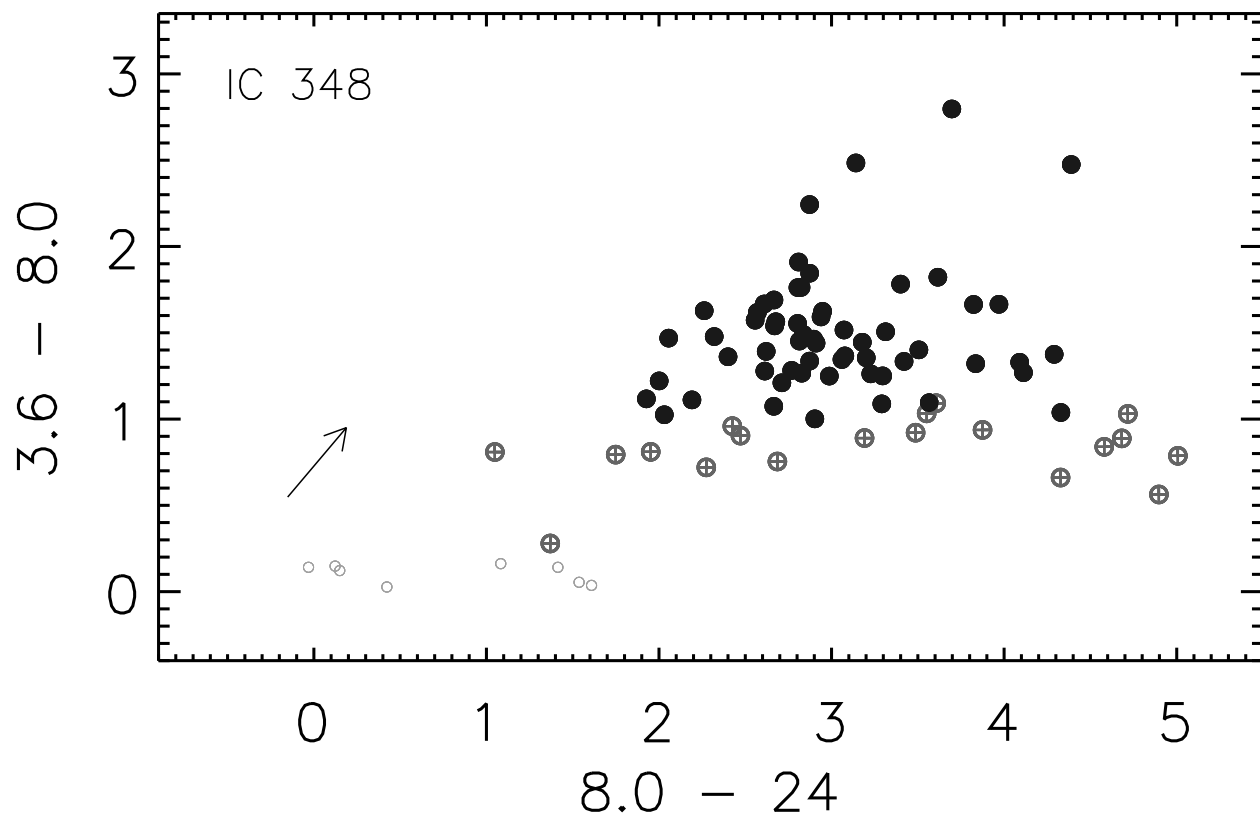


Fig. 7.— IRAC-MIPS color-color diagram for IC 348 sources detected at  $24\ \mu\text{m}$ . Small open circles indicate diskless stars, circled crosses indicate anemic disks and solid filled circles denote stars with thick disks. This figure shows that four early type stars that appear naked or diskless in IRAC colors show significant MIPS  $24\ \mu\text{m}$  excess possibly indicating the presence of a debris disk. Stars with anemic disks form a narrow horizontal band marking the lower bound of the extent of thick disk sources. Six anemic disks with the largest  $24\ \mu\text{m}$  excess are likely disks with holes or significantly depleted inner regions. A reddening vector of length  $A_V = 20$  magnitude is shown.

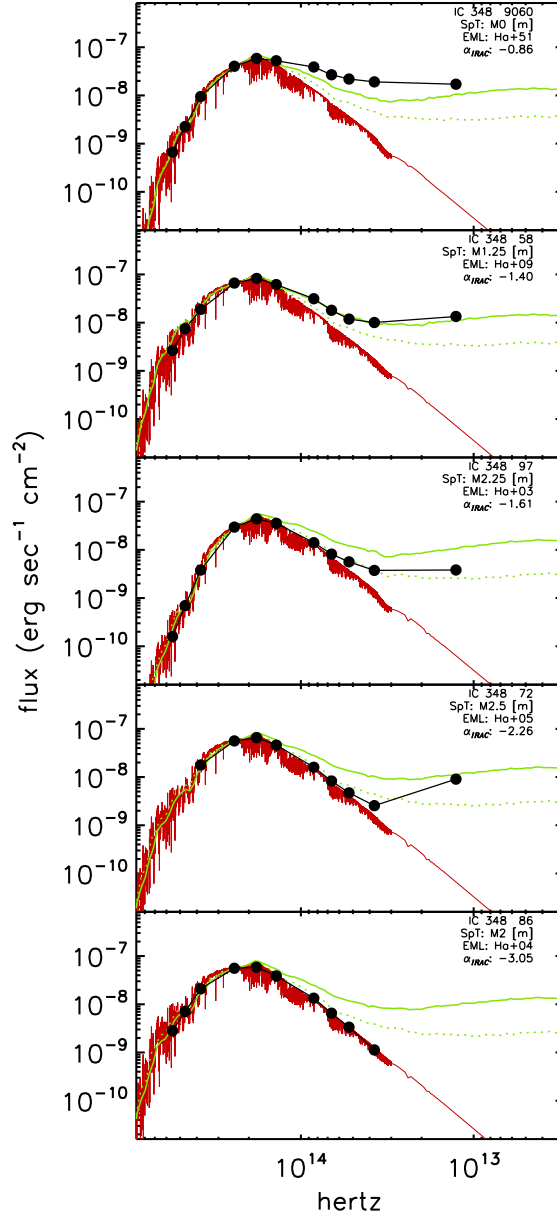


Fig. 8.— Disk Evolution. SEDs for five M stars in the cluster exhibiting differing levels of infrared excess and disk emission, ranging from a system with a robust excess and highly flared disk structure through systems with modest infrared excesses and flatter disk structures to a diskless star. Plotted for comparison are the corresponding synthetic stellar photospheric models (red jagged line) and two disk models whose scale heights differ. The upper disk model (solid line) has a scale height appropriate for a disk in hydrostatic equilibrium, while the lower disk model (dotted line) has its scale height reduced by a factor of 3. The lower disk scale height corresponds to a situation in which emitting dust has settled toward the mid-plane.

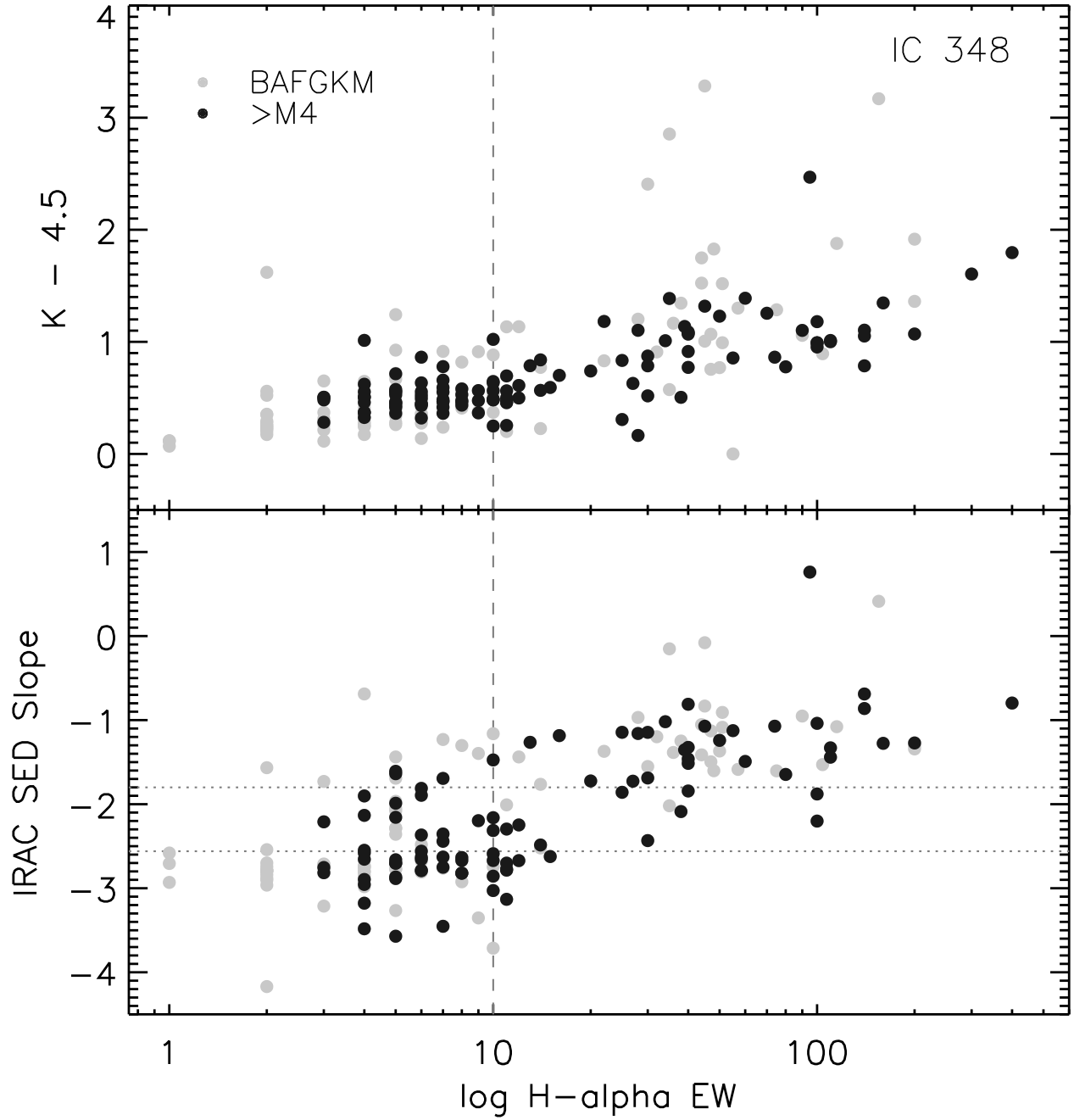


Fig. 9.— Plot of the relation between  $H\alpha$  equivalent width and  $IRAC$  SED (dereddened) power-law slope. Sources with disks are the strongest  $H\alpha$  emitters indicating a link between accretion and the presence of a dusty, optically thick circumstellar disk.

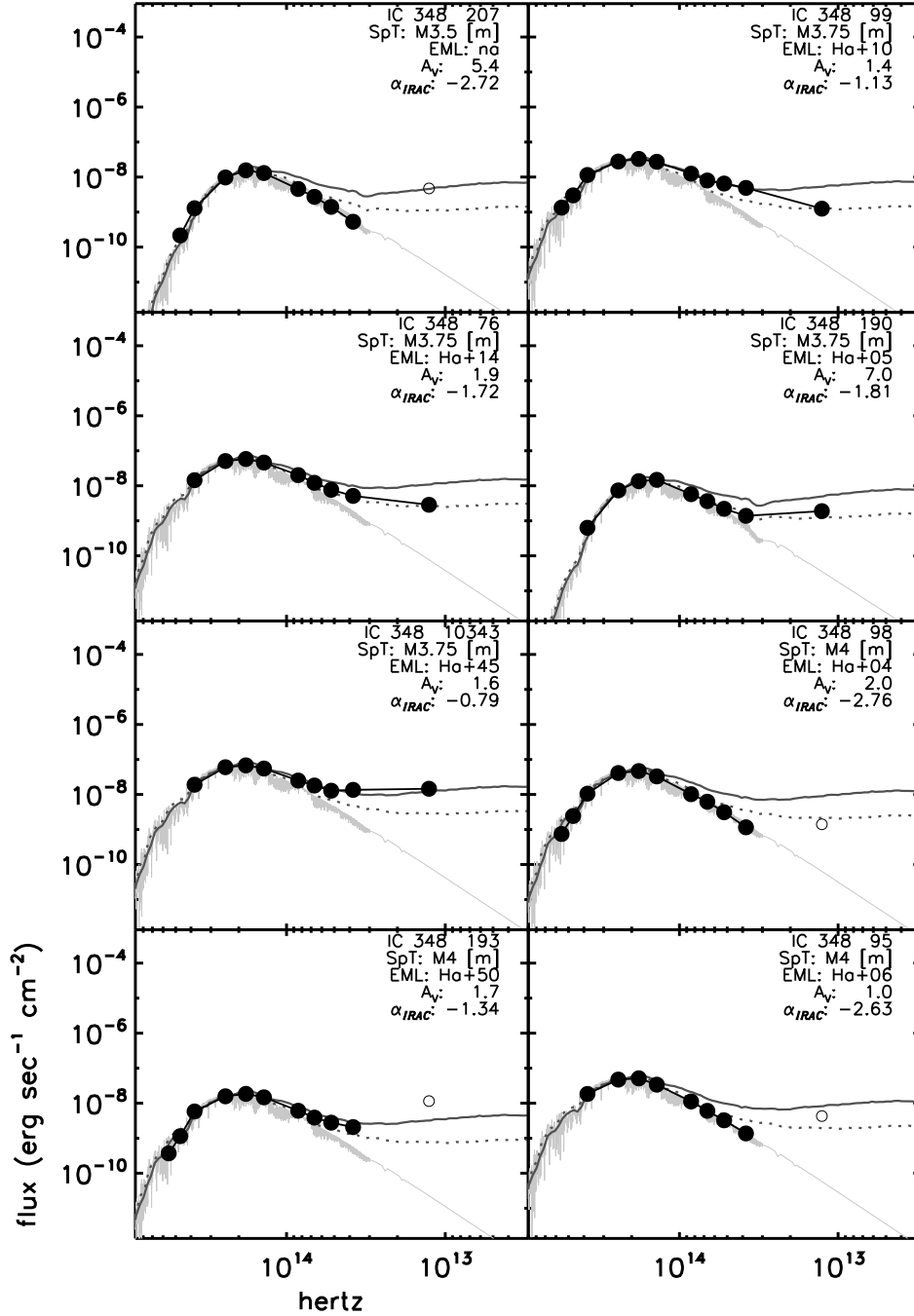


Fig. A-1.— Atlas of Observed Spectral Energy Distributions for members of the 2-3 Myr IC 348 cluster. SAMPLE PAGE. Astrographical ( $A_V$ ,  $\alpha_{IRAC}$ , Spectral type, etc) information is given for each member. The best fit appropriately reddened model atmosphere is overplotted as are two reddened disk models with different disk scale heights. The underlying photosphere of the disk models were varied according to the spectral type of the IC 348 member. Filled circles represent the detected fluxes and open circles upper limits to the observed fluxes. Error bars are also plotted but in almost all cases are smaller than the plotted circles. See Appendix A and text. (Complete catalog of SEDs and complete electronic tabular material can be obtained at: [http://www.cfa.harvard.edu/~clada/pubs\\_html/ic348\\_spitzer.html](http://www.cfa.harvard.edu/~clada/pubs_html/ic348_spitzer.html)).



Table 1. *Spitzer* IRAC/MIPS IC 348 Catalog

No.	R.A. (J2000)	Dec. (J2000)	IRAC Photometry								MIPS Photometry		Blend Flags	
			3.6	err	4.5	err	5.8	err	8.0	err	24	err <sup>(a)</sup>	IRAC <sup>(b)</sup>	MIPS <sup>(c)</sup>
1	03:44:34.212	32:09:46.69	6.74	0.01	6.54	0.02	6.58	0.02	6.50	0.03	0.89	-9.00		
2	03:44:35.364	32:10:04.58	7.09	0.02	6.81	0.02	6.46	0.04	5.82	0.04	3.20	0.03		
3	03:44:50.649	32:19:06.75	7.53	0.01	7.61	0.03	7.47	0.04	7.50	0.04	7.08	0.05		
4	03:44:31.188	32:06:22.09	7.79	0.01	7.74	0.02	7.66	0.02	7.73	0.03	4.38	-9.00		
5	03:44:26.027	32:04:30.41	6.97	0.01	6.52	0.01	6.32	0.02	5.63	0.02	2.76	0.03		
6	03:44:36.941	32:06:45.37	7.92	0.02	7.70	0.01	7.53	0.05	7.12	0.03	5.37	0.04		
7	03:44:08.476	32:07:16.50	8.54	0.01	8.60	0.01	8.53	0.03	8.48	0.03	6.95	0.05		
8	03:44:09.152	32:07:09.33	8.61	0.01	8.62	0.01	8.52	0.03	8.33	0.04	6.96	0.06		
9	03:44:39.178	32:09:18.35	8.47	0.01	8.41	0.02	8.35	0.03	8.50	0.10	4.14	-9.00		
10	03:44:24.664	32:10:15.04	8.71	0.02	8.67	0.01	8.64	0.03	8.68	0.04	4.81	-9.00		
11	03:45:07.965	32:04:02.09	8.59	0.01	8.63	0.01	8.44	0.06	8.44	0.01	8.32	0.04		
13	03:43:59.641	32:01:54.17	7.22	0.01	6.42	0.01	5.83	0.03	4.98	0.04	2.11	0.03		
15	03:44:44.716	32:04:02.72	8.52	0.01	8.17	0.03	7.81	0.03	7.17	0.02	4.11	0.03		
16	03:44:32.743	32:08:37.46	9.36	0.01	9.37	0.03	9.22	0.06	9.27	0.12	5.42	-9.00		
17	03:44:47.724	32:19:11.95	9.25	0.01	9.11	0.01	9.21	0.05	9.12	0.08	6.13	-9.00		

<sup>(a)</sup>If the MIPS 24 $\mu$ m magnitude error corresponds to  $-9$  then the MIPS 24 $\mu$ m flux is a 95% upper limit. See text.

<sup>(b)</sup>IRAC blend flag.

<sup>(c)</sup>MIPS blend flag.

Note. — The complete version of this table is in the electronic edition of the Journal. The printed edition contains only this sample.

Note. — This table is available only on-line as a machine-readable table.

Table 2. SED derived *IRAC*  $\alpha$  and  $A_V$

No.	SpT	$A_V^{(a)}$		$\alpha_{IRAC}$		Fits <sup>(b)</sup>		N(bands)	Disk Type <sup>(c)</sup>
		[mag	$\alpha_0$	$1\sigma$	$\alpha_d$	$1\sigma$			
1	B5	3.1	-2.638	0.102	-2.708	0.091	4	STAR	
2	A2	3.2	-1.396	0.127	-1.468	0.143	4	THICK	
3	A0	3.9	-2.794	0.110	-2.883	0.115	4	STAR	
4	F0	2.3	-2.786	0.091	-2.838	0.082	4	STAR	
5	G8	7.7	-1.389	0.160	-1.563	0.177	4	THICK	
6	G3	3.5	-1.972	0.079	-2.051	0.094	4	ANEMIC	
7	A0	1.7	-2.788	0.071	-2.826	0.078	4	STAR	
8	A2	1.6	-2.532	0.101	-2.569	0.109	4	ANEMIC	
9	G8	5.3	-2.894	0.134	-3.014	0.112	4	STAR	
10	F2	2.1	-2.827	0.054	-2.875	0.044	4	STAR	
11	G4	6.0	-2.653	0.114	-2.789	0.121	4	STAR	
13	M0.5	19.0	-0.315	0.115	-0.744	0.056	4	THICK	
15	M0.5	2.5	-1.325	0.088	-1.382	0.100	4	THICK	
16	G6	3.0	-2.724	0.098	-2.792	0.095	4	STAR	
17	A4	5.0	-2.772	0.098	-2.885	0.091	4	STAR	

<sup>(a)</sup> $A_V$  derived from SED fitting with model atmospheres; see text.

<sup>(b)</sup>*IRAC*  $\alpha$  fits.  $\alpha_0$ : Observed slope;  $\alpha_d$ : Dereddened slope

<sup>(c)</sup>Disk Type based upon  $\alpha_d$

Note. — The complete version of this table is in the electronic edition of the Journal. The printed edition contains only this sample.

Note. — This table is available only on-line as a machine-readable table.

Table 3. Median IC 348 Star/Disk Spectral Energy Distributions

Measurement	$V_L$	$R_C$	$I_C$	$J$	$H$	$K_s$	3.6	4.5	5.8	8.0	24
AF Spectral Types											
<b>Stars</b>											
magnitudes	11.588	...	10.304	9.343	8.997	8.821	8.749	8.737	8.655	8.727	7.194
median [log] flux	-6.312	...	-6.148	-6.139	-6.322	-6.552	-7.121	-7.408	-7.663	-8.106	-8.902
$1\sigma; (N_{stars})$	-7.027(3)	... (0)	-7.366(6)	... (7)	-8.009(7)	-8.047(7)	-8.416(7)	-8.665(7)	-8.850(7)	-9.179(7)	-9.393(4)
<b>Anemic Disks</b>											
magnitudes	...	...	10.392	9.343	9.040	8.797	8.696	8.695	8.554	8.373	6.982
median [log] flux	...	...	-6.184	-6.139	-6.339	-6.542	-7.100	-7.391	-7.623	-7.964	-8.817
$1\sigma; (N_{stars})$	... (0)	... (0)	... (1)	... (1)	... (1)	... (1)	... (1)	... (1)	... (1)	... (1)	... (1)
<b>Thick Disks</b>											
magnitudes	11.731	11.133	10.299	9.343	9.000	8.776	8.640	8.463	8.028	7.051	4.267
median [log] flux	-6.368	-6.287	-6.147	-6.139	-6.323	-6.533	-7.077	-7.298	-7.413	-7.435	-7.731
$1\sigma; (N_{stars})$	... (1)	... (1)	-7.195(2)	... (2)	-8.011(2)	-7.800(2)	-8.410(2)	-8.107(2)	-8.629(2)	-8.091(2)	-8.201(2)
G Spectral Types											
<b>Stars</b>											
magnitudes	13.843	12.801	11.881	10.195	9.451	9.168	8.998	8.979	8.892	8.932	8.681
median [log] flux	-7.213	-6.954	-6.779	-6.480	-6.504	-6.690	-7.220	-7.504	-7.758	-8.188	-9.496
$1\sigma; (N_{stars})$	-8.484(3)	-8.127(3)	-7.970(6)	... (6)	-8.007(6)	-7.988(6)	-8.410(6)	-8.654(6)	-8.955(6)	-9.092(6)	-9.629(3)
<b>Anemic Disks</b>											
magnitudes	13.749	12.771	11.813	10.195	9.308	8.853	8.345	8.128	8.100	7.449	3.118
median [log] flux	-7.176	-6.942	-6.752	-6.480	-6.446	-6.564	-6.959	-7.164	-7.441	-7.595	-7.271
$1\sigma; (N_{stars})$	... (1)	-8.069(2)	-7.685(2)	... (2)	-7.265(2)	-7.124(2)	-7.339(2)	-7.544(2)	-7.911(2)	-7.922(2)	-7.293(2)
<b>Thick Disks</b>											
magnitudes	13.343	12.488	11.763	10.195	9.252	8.672	7.634	7.207	7.024	6.347	3.515
median [log] flux	-7.013	-6.829	-6.732	-6.480	-6.424	-6.492	-6.675	-6.795	-7.011	-7.154	-7.430
$1\sigma; (N_{stars})$	... (1)	... (1)	... (1)	... (1)	... (1)	... (1)	... (1)	... (1)	... (1)	... (1)	... (1)
K0–K6 Spectral Types											
<b>Stars</b>											
magnitudes	15.154	14.078	13.035	11.360	10.528	10.263	10.131	10.069	10.026	10.007	...

Table 3—Continued

Measurement	$V_L$	$R_C$	$I_C$	$J$	$H$	$K_s$	3.6	4.5	5.8	8.0	24
median [log] flux	-7.738	-7.465	-7.241	-6.946	-6.934	-7.128	-7.673	-7.941	-8.212	-8.618	...
$1\sigma$ ; ( $N_{stars}$ )	-8.786(9)	-8.412(9)	-8.256(13)	... (13)	-8.682(12)	-8.682(13)	-9.009(13)	-9.192(13)	-9.347(13)	-9.688(13)	... (0)
<b>Anemic Disks</b>											
magnitudes	...	...	13.004	11.360	10.509	10.091	9.695	9.528	9.525	8.994	4.337
median [log] flux	...	...	-7.228	-6.946	-6.927	-7.060	-7.499	-7.724	-8.012	-8.213	-7.759
$1\sigma$ ; ( $N_{stars}$ )	... (0)	... (0)	... (1)	... (1)	... (1)	... (1)	... (1)	... (1)	... (1)	... (1)	... (1)
<b>Thick Disks</b>											
magnitudes	...	...	...	...	...	...	...	...	...	...	...
median [log] flux	...	...	...	...	...	...	...	...	...	...	...
$1\sigma$ ; ( $N_{stars}$ )	... (0)	... (0)	... (0)	... (0)	... (0)	... (0)	... (0)	... (0)	... (0)	... (0)	... (0)
K6–M0 Spectral Types											
<b>Stars</b>											
magnitudes	16.812	15.346	13.969	11.931	10.903	10.541	10.327	10.247	10.181	10.306	10.031
median [log] flux	-8.401	-7.972	-7.614	-7.174	-7.085	-7.239	-7.752	-8.012	-8.274	-8.737	-10.036
$1\sigma$ ; ( $N_{stars}$ )	-9.315(3)	-8.884(4)	-8.489(5)	... (5)	-8.324(5)	-8.404(5)	-8.736(5)	-8.956(5)	-9.092(5)	-9.427(5)	... (1)
<b>Anemic Disks</b>											
magnitudes	16.894	15.479	14.148	11.931	10.924	10.561	10.271	10.246	10.051	9.651	...
median [log] flux	-8.434	-8.025	-7.686	-7.174	-7.093	-7.248	-7.730	-8.011	-8.222	-8.475	...
$1\sigma$ ; ( $N_{stars}$ )	... (1)	... (1)	... (1)	... (1)	... (1)	... (1)	... (1)	... (1)	... (1)	... (1)	... (0)
<b>Thick Disks</b>											
magnitudes	16.719	15.435	14.084	11.931	10.812	10.252	9.455	9.055	8.715	8.001	4.990
median [log] flux	-8.364	-8.007	-7.660	-7.174	-7.048	-7.124	-7.403	-7.535	-7.688	-7.816	-8.020
$1\sigma$ ; ( $N_{stars}$ )	-9.516(5)	-8.853(5)	-8.352(7)	... (7)	-8.312(7)	-7.986(7)	-7.916(7)	-7.924(7)	-8.182(7)	-8.492(7)	-8.345(7)
M0–M2 Spectral Types											
<b>Stars</b>											
magnitudes	17.725	16.277	14.682	12.557	11.583	11.269	11.046	11.036	10.970	10.921	...
median [log] flux	-8.766	-8.344	-7.900	-7.425	-7.357	-7.531	-8.040	-8.327	-8.590	-8.984	...
$1\sigma$ ; ( $N_{stars}$ )	-10.277(5)	-9.636(5)	-8.775(12)	... (13)	-8.882(12)	-8.926(12)	-9.263(12)	-9.532(12)	-9.766(12)	-10.139(12)	... (0)
<b>Anemic Disks</b>											
magnitudes	17.633	16.138	14.657	12.557	11.561	11.216	10.993	10.936	10.793	10.704	4.974
median [log] flux	-8.729	-8.289	-7.890	-7.425	-7.348	-7.510	-8.019	-8.287	-8.519	-8.896	-8.013

Table 3—Continued

Measurement	$V_L$	$R_C$	$I_C$	$J$	$H$	$K_s$	3.6	4.5	5.8	8.0	24
$1\sigma; (N_{stars})$	-10.670(3)	-9.384(3)	-8.817(4)	... (4)	-9.027(4)	-9.012(4)	-8.963(4)	-9.098(4)	-9.352(4)	-9.285(4)	... (1)
<b>Thick Disks</b>											
magnitudes	17.568	16.135	14.503	12.557	11.537	10.989	10.280	9.895	9.584	8.880	5.433
median [log] flux	-8.704	-8.287	-7.828	-7.425	-7.338	-7.419	-7.733	-7.871	-8.035	-8.167	-8.197
$1\sigma; (N_{stars})$	-9.436(7)	-8.933(7)	-8.351(15)	... (15)	-8.503(14)	-8.043(14)	-7.956(14)	-8.072(13)	-8.586(11)	-8.444(12)	-8.428(12)
M2–M3 Spectral Types											
<b>Stars</b>											
magnitudes	18.151	16.658	14.906	12.816	11.854	11.549	11.241	11.236	11.198	11.184	...
median [log] flux	-8.937	-8.497	-7.989	-7.528	-7.465	-7.643	-8.118	-8.407	-8.681	-9.088	...
$1\sigma; (N_{stars})$	-10.015(8)	-9.552(8)	-8.864(11)	... (12)	-8.965(12)	-9.098(12)	-9.371(12)	-9.639(12)	-9.696(12)	-10.203(12)	... (0)
<b>Anemic Disks</b>											
magnitudes	18.014	16.565	14.919	12.816	11.836	11.500	11.274	11.180	11.120	10.931	5.773
median [log] flux	-8.882	-8.459	-7.994	-7.528	-7.458	-7.623	-8.131	-8.385	-8.650	-8.987	-8.333
$1\sigma; (N_{stars})$	-9.908(2)	-9.772(4)	-9.077(7)	... (7)	-8.888(7)	-8.739(7)	-8.692(7)	-8.820(7)	-8.978(7)	-9.429(7)	... (1)
<b>Thick Disks</b>											
magnitudes	18.228	16.733	14.783	12.816	11.817	11.482	10.862	10.704	10.450	9.518	6.463
median [log] flux	-8.967	-8.527	-7.940	-7.528	-7.450	-7.616	-7.966	-8.194	-8.381	-8.422	-8.609
$1\sigma; (N_{stars})$	-9.803(5)	-9.401(5)	-8.650(7)	... (7)	-8.772(7)	-8.205(7)	-8.092(7)	-8.120(7)	-8.214(7)	-8.361(7)	-8.623(6)
M3–M4 Spectral Types											
<b>Stars</b>											
magnitudes	18.466	16.957	14.924	12.889	11.966	11.653	11.418	11.322	11.275	11.345	...
median [log] flux	-9.063	-8.616	-7.996	-7.558	-7.510	-7.684	-8.188	-8.442	-8.712	-9.153	...
$1\sigma; (N_{stars})$	-10.046(3)	-9.551(3)	-8.764(12)	... (12)	-8.797(12)	-8.900(12)	-9.343(12)	-9.549(12)	-9.771(12)	-10.001(12)	... (0)
<b>Anemic Disks</b>											
magnitudes	18.278	16.791	14.887	12.889	11.926	11.486	11.261	11.177	10.952	10.680	6.599
median [log] flux	-8.987	-8.550	-7.982	-7.558	-7.494	-7.618	-8.126	-8.384	-8.582	-8.887	-8.664
$1\sigma; (N_{stars})$	-9.699(3)	-9.313(4)	-8.791(5)	... (5)	-8.705(5)	-8.574(5)	-8.676(5)	-8.730(5)	-8.784(5)	-9.167(5)	... (1)
<b>Thick Disks</b>											
magnitudes	18.209	16.888	14.964	12.889	11.991	11.489	10.809	10.452	10.021	9.123	6.342
median [log] flux	-8.960	-8.589	-8.012	-7.558	-7.519	-7.619	-7.945	-8.094	-8.210	-8.264	-8.561
$1\sigma; (N_{stars})$	... (1)	... (1)	-8.669(7)	... (7)	-8.599(7)	-8.338(7)	-8.377(7)	-8.473(7)	-8.544(7)	-8.675(7)	-8.762(7)

Table 3—Continued

Measurement	$V_L$	$R_C$	$I_C$	$J$	$H$	$K_s$	3.6	4.5	5.8	8.0	24
M4–M5 Spectral Types											
<b>Stars</b>											
magnitudes	19.801	18.265	16.085	13.687	12.761	12.359	12.016	11.947	11.915	11.896	...
median [log] flux	-9.597	-9.139	-8.461	-7.877	-7.827	-7.967	-8.428	-8.692	-8.967	-9.373	...
$1\sigma$ ; ( $N_{stars}$ )	-10.841(6)	-9.853(9)	-9.400(26)	... (27)	-9.305(25)	-9.457(25)	-9.590(26)	-9.812(26)	-9.954(26)	-10.258(25)	... (0)
<b>Anemic Disks</b>											
magnitudes	19.966	18.392	16.136	13.687	12.781	12.380	12.037	11.943	11.861	11.553	8.566
median [log] flux	-9.663	-9.190	-8.481	-7.877	-7.836	-7.975	-8.436	-8.690	-8.946	-9.236	-9.450
$1\sigma$ ; ( $N_{stars}$ )	-10.335(8)	-9.795(11)	-9.222(15)	... (16)	-8.890(16)	-8.833(16)	-9.261(15)	-9.522(15)	-9.749(14)	-9.921(12)	-9.313(4)
<b>Thick Disks</b>											
magnitudes	19.793	18.181	16.138	13.687	12.727	12.254	11.685	11.447	11.164	10.507	7.393
median [log] flux	-9.593	-9.106	-8.482	-7.877	-7.814	-7.925	-8.295	-8.492	-8.667	-8.818	-8.981
$1\sigma$ ; ( $N_{stars}$ )	-10.426(8)	-9.647(12)	-9.093(18)	... (19)	-9.016(19)	-8.783(19)	-9.174(19)	-9.208(19)	-9.338(18)	-9.366(17)	-9.309(14)
M5–M6 Spectral Types											
<b>Stars</b>											
magnitudes	21.230	19.424	16.873	14.345	13.529	13.115	12.718	12.619	12.603	12.886	...
median [log] flux	-10.168	-9.603	-8.776	-8.140	-8.135	-8.269	-8.708	-8.961	-9.243	-9.769	...
$1\sigma$ ; ( $N_{stars}$ )	-10.588(7)	-10.106(12)	-9.573(16)	... (16)	-9.391(16)	-9.782(15)	-9.695(15)	-9.933(16)	-10.159(16)	-10.272(14)	... (0)
<b>Anemic Disks</b>											
magnitudes	21.148	19.332	16.923	14.345	13.543	13.119	12.726	12.564	12.537	12.233	9.628
median [log] flux	-10.136	-9.566	-8.796	-8.140	-8.141	-8.271	-8.711	-8.938	-9.216	-9.508	-9.875
$1\sigma$ ; ( $N_{stars}$ )	-10.791(8)	-10.105(16)	-9.650(25)	... (28)	-9.549(26)	-9.481(27)	-9.523(28)	-9.704(27)	-9.946(25)	-10.198(23)	-10.172(2)
<b>Thick Disks</b>											
magnitudes	21.042	19.171	16.852	14.345	13.521	13.064	12.579	12.276	11.923	11.123	7.830
median [log] flux	-10.093	-9.502	-8.768	-8.140	-8.131	-8.249	-8.653	-8.823	-8.971	-9.064	-9.156
$1\sigma$ ; ( $N_{stars}$ )	-10.676(6)	-10.238(11)	-9.757(17)	... (19)	-9.439(18)	-9.580(18)	-9.478(18)	-9.528(18)	-9.620(17)	-9.647(17)	-9.409(8)
M6+ Spectral Types											
<b>Stars</b>											
magnitudes	24.453	22.512	19.810	16.562	15.731	15.170	14.688	14.574	14.533	14.478	...

Table 3—Continued

Measurement	$V_L$	$R_C$	$I_C$	$J$	$H$	$K_s$	3.6	4.5	5.8	8.0	24
median [log] flux	-11.458	-10.838	-9.951	-9.027	-9.016	-9.091	-9.496	-9.742	-10.015	-10.406	...
$1\sigma; (N_{stars})$	-12.041(2)	-11.551(5)	-10.778(8)	... (8)	-10.365(8)	-10.508(8)	-10.293(8)	-10.594(8)	-10.964(6)	-12.237(3)	... (0)
<b>Anemic Disks</b>											
magnitudes	...	22.497	19.621	16.562	15.667	15.120	14.592	14.429	14.060	13.977	9.669
median [log] flux	...	-10.832	-9.875	-9.027	-8.990	-9.071	-9.458	-9.685	-9.826	-10.206	-9.892
$1\sigma; (N_{stars})$	... (0)	-11.673(3)	-10.531(15)	... (15)	-10.153(15)	-10.079(15)	-10.292(14)	-10.471(14)	-10.349(7)	-11.134(3)	... (1)
<b>Thick Disks</b>											
magnitudes	...	22.504	19.765	16.562	15.710	15.159	14.390	13.982	13.493	12.724	9.965
median [log] flux	...	-10.835	-9.933	-9.027	-9.007	-9.087	-9.377	-9.506	-9.599	-9.705	-10.010
$1\sigma; (N_{stars})$	... (0)	-11.718(4)	-10.543(11)	... (11)	-10.359(10)	-10.150(11)	-9.916(11)	-10.013(11)	-10.089(8)	-10.167(8)	-10.964(2)

Table 4. Passbands

Passband	Data		Flux Conversion		
	System <sup>(a)</sup>	Source	$\lambda_0$ ( $\mu\text{m}$ )	$F_\nu$ (Jy)	Ref.
$V_L$	Landolt	1,2,3	0.5423	3723.	9
$R_C$	Cousins	1,2,3	0.6410	3064.	10
$I_C$	Cousins	1,2,3	0.7890	2416.	10
$J$	2MASS	4,5,6,7	1.235	1594.	11
$H$	2MASS	4,5,6,7	1.662	1024.	11
$K_s$	2MASS	4,5,6,7	2.159	666.8	11
3.6	<i>IRAC</i>	8	3.550	280.9	12
4.5	<i>IRAC</i>	8	4.493	179.5	12
5.8	<i>IRAC</i>	8	5.731	115.0	12
8.0	<i>IRAC</i>	8	7.872	64.13	12
24	<i>MIPS</i>	8	23.68	7.3	13

<sup>(a)</sup>Photometric system assumed for the conversion from magnitude to flux. For example, all the near-infrared data obtained from the FLAMINGOS instrument was zeropoint calibrated to 2MASS even though no formal color terms were included in that magnitude calibration. Similarly, it is assumed that the Cousins filter transmissions from 3 different surveys were identical.

References. — : 1: Herbig (1998); 2: Luhman et al. (1998); 3: Luhman (1999); 4: Cutri et al. (2003); 5: Muench et al. (2003); 6: Luhman et al. (2003); 7: Luhman et al. (2005); 8: This paper; 9: Cohen et al. (2003); 10: Bessell et al. (1998); 11: Cohen et al. (2003); 12: Reach et al. (2005); 13: SSC.